HHS Public Access

Author manuscript

Cell Rep. Author manuscript; available in PMC 2020 October 27.

Published in final edited form as:

Cell Rep. 2020 October 13; 33(2): 108266. doi:10.1016/j.celrep.2020.108266.

FMRP-PKA Activity Negative Feedback Regulates RNA Binding-Dependent Fibrillation in Brain Learning and Memory Circuitry

James C. Sears[1,2,*], **Kendal Broadie**[1,2,3,4,5,*]

[1]Vanderbilt Brain Institute, Vanderbilt University Medical Center, Nashville, TN 37235, USA

[2]Department of Biological Sciences, Vanderbilt University, Nashville, TN 37235, USA

[3]Department of Pharmacology, Vanderbilt University Medical Center, Nashville, TN 37235, USA

[4]Department of Cell and Developmental Biology, Vanderbilt University Medical Center, Nashville, TN 37235, USA

[5]Lead Contact

SUMMARY

Fragile X mental retardation protein (FMRP) promotes cyclic AMP (cAMP) signaling. Using an *in vivo* protein kinase A activity sensor (PKA-SPARK), we find that *Drosophila* FMRP (dFMRP) and human FMRP (hFMRP) enhance PKA activity in a central brain learning and memory center. Increasing neuronal PKA activity suppresses FMRP in Kenyon cells, demonstrating an FMRP-PKA negative feedback loop. A patient-derived R140Q FMRP point mutation mislocalizes PKA-SPARK activity, whereas deletion of the RNA-binding argi-nine-glycine-glycine (RGG) box (hFMRP-ΔRGG) produces fibrillar PKA-SPARK assemblies colocalizing with ribonucleoprotein (RNP) and aggregation (thioflavin T) markers, demonstrating fibrillar partitioning of cytosolic protein aggregates. hFMRP-ΔRGG reduces dFMRP levels, indicating RGG-independent regulation. Short-term hFMRP-ΔRGG induction produces activated PKA-SPARK puncta, whereas long induction drives fibrillar assembly. Elevated temperature disassociates hFMRP-ΔRGG aggregates and blocks activated PKA-SPARK localization. These results suggest that FMRP regulates compartmentalized signaling via complex assembly, directing PKA activity localization, with FMRP RGG box RNA binding restricting separation via low-complexity interactions.

Graphical Abstract

*Correspondence: james.c.sears@vanderbilt.edu (J.C.S.), kendal.broadie@vanderbilt.edu (K.B.).

AUTHOR CONTRIBUTIONS

Methodology, Investigation, and Software, J.C.S.; Conceptualization, Writing, and Funding Acquisition, J.C.S. and K.B.

SUPPLEMENTAL INFORMATION

Supplemental Information can be found online at https://doi.org/10.1016/j.celrep.2020.108266.

DECLARATION OF INTERESTS

The authors declare no competing interests.

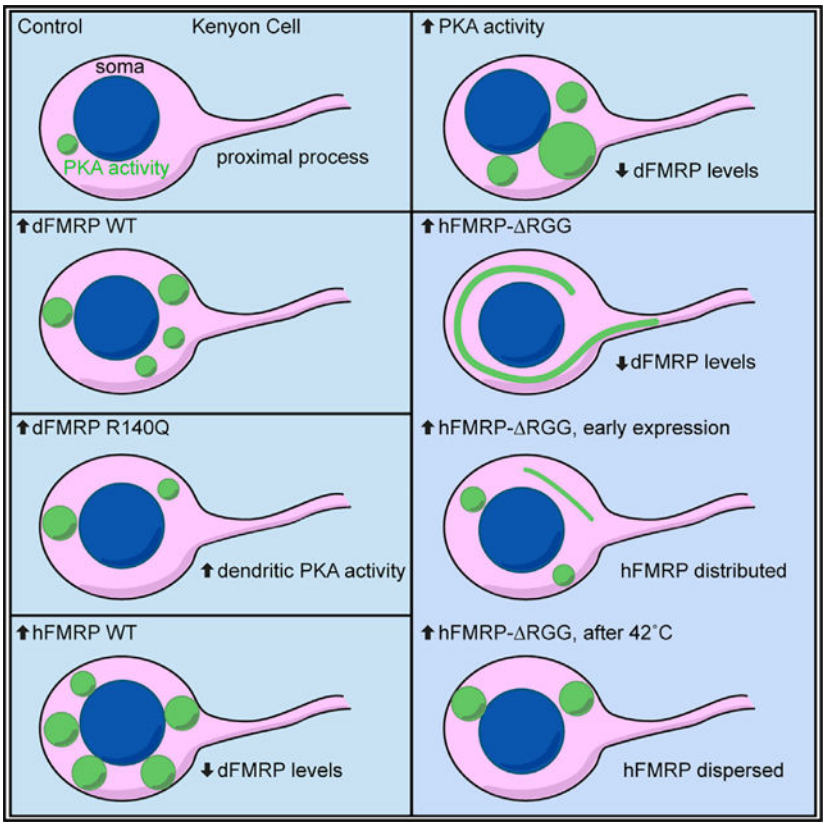

In Brief

FMRP is required for brain cAMP induction and cAMP-dependent PKA activation, but the FMRP mechanism is uncharacterized. Sears and Broadie test FXS patient-derived and FMRP domain-deficient mutants to reveal conserved FMRP functions regulating PKA activation, subcellular localization, and reversible partitioning into elongated fibrillar assemblies in brain learning/memory circuit neurons.

INTRODUCTION

Fragile X syndrome (FXS) is the most common heritable intellectual disability and autism spectrum disorder. Fragile X mental retardation protein (FMRP) is a conserved translational regulator with mRNA binding-dependent and -independent functions (Davis and Broadie, 2017). To elucidate FMRP domain roles, we use FXS patient-derived mutations and domain-deleted FMRP variants in the Drosophila mushroom body (MB) learning/memory brain center. It is known that FMRP promotes cyclic AMP (cAMP) induction from human to Drosophila brains (Berry-Kravis and Huttenlocher, 1992; Berry-Kravis et al., 1995; Kelley et al.,2007) and that cAMP acts upstream of protein kinase A (PKA) to mediate MB-dependent learning acquisition and memory consolidation (Blum et al., 2009; Zars et al., 2000). FMRP also positively regulates translation of the PKA anchor Rugose/Neurobeachin (NBEA) via direct mRNA binding (Sears et al., 2019). Importantly, this PKA anchor mediates MB-dependent learning and memory (Volders et al., 2012). FMRP drives PKA

activation in the MB, as demonstrated with the in vivo PKA activity biosensor PKA-SPARK (Sears et al., 2019; Zhang et al., 2018). In the current study, we pursue this mechanism using Drosophila and human FMRP variants targeted to the MB circuit, assaying effects on PKA-SPARK signaling.

Epigenetic FMRP silencing is the common cause of FXS (Verkerk et al., 1991), but coding alleles also produce FXS (Coffee et al., 2008; Collins et al., 2010). Patient-derived point mutations affect mRNA binding-dependent and -independent functions (Myrick et al., 2014, 2015a). A key example is R138Q (Drosophila R140Q), which causes neural circuit defects without affecting RNA binding regulation (Collins et al., 2010; Myrick et al., 2015a). The conserved protein-protein interaction domain has critical mRNA binding-independent FMRP functions (Hu et al., 2015; Myrick et al., 2015a, 2015b). Other FMRP domains have implied central roles based on biochemical binding studies. A key example is the arginine-glycine-glycine (RGG) box, which binds transcripts with G-quadruplex secondary structures (Ozdilek et al., 2017). Immediately adjacent to the RGG box, low-complexity (LC) domains mediate mRNA binding and fibrillization (Molliex et al., 2015). Although LC domain-dependent fibrillization is well documented in vitro to drive elongated protein assemblies (Kato et al., 2012), with LC domains in CPEB/Orb2 shown recently to form amyloid filaments in memory-associated processes (Hervas et al., 2020; Si and Kandel, 2016), the functional in vivo relevance of neuronal LC domains remains an important open question (Alberti et al., 2019).

Here we test disease-associated R140Q-and RGG box-deficient FMRP roles in the Drosophila brain MB learning/memory circuit. We find that R140Q promotes aberrant PKA activity in dendritic arbors, generates oxidative stress, and disrupts Kenyon cell architecture. These results show an FMRP mRNA binding-independent role of PKA activation and R140Q mutant defects elsewhere (Myrick et al., 2015a). We find that human FMRP (hFMRP) increases PKA activity and suppresses endogenous *Drosophila* FMRP (dFMRP) expression, demonstrating a negative feedback loop limiting FMRP expression. Consistent with a PKA-dependent feedback mechanism, we find that increasing PKA activity also suppresses FMRP levels. We find that hFMRP lacking the RGG domain also reduces dFMRP, showing an mRNA-binding independent mechanism. Surprisingly, hFMRP-ΔRGG causes striking fibrillar assemblies with colocalized PKA activity in Kenyon cells, with time-dependent dynamics and heat dispersal characteristics of LC interactions. This study shows that FMRP self-regulates and also mediates PKA activity localization in a negative feedback loop via an mRNA binding-dependent mechanism in brain learning and memory circuit neurons.

RESULTS

Disease-Associated dFMRP and hFMRP Variants Differentially Promote PKA Activity

The MB contains two bilateral groups of Kenyon cells, with dorsal somata (Figure 1A, left), MB calyx dendritic arbors (Figure 1A, center), and distinctive axon lobes (Figure 1A, right). In the MB, cAMP signaling via PKA is required for learning and memory (Blum et al., 2009; Zars et al., 2000). FXS models show a reduction in cAMP induction (Berry-Kravis and Huttenlocher, 1992; Berry-Kravis et al., 1995; Kelley et al., 2007). FMRP loss of

function (LOF) reduces PKA activity, and FMRP overexpression (OE) increases PKA activity in Kenyon cells (Sears et al., 2019), based on PKA-SPARK, a GFP biosensor that generates reversible oligomer fluorescent puncta (Zhang et al., 2018). We hypothesize that disease-associated and domain-altered FMRP variants should reveal mechanisms of this PKA-SPARK activation. To test this idea, we used the binary Gal4/UAS system for MB-targeted expression of six transgenic constructs; UAS-*dfmr1* RNAi (Doll and Broadie, 2015), *UAS-dfmr1* wild type (WT) + UAS-dfmr1-R140Q (Myrick et al., 2015a), *UAS-hFMR*^{ISO7} (hFMRP) + *UAS-hFMR1*^{iso6} (hFMRP full length [FL]) + UAS-*hFMR1-ΔRGG* (Coffee, 2011; Coffee et al., 2010), all driven with the MB-specific OK107-Gal4 (Connolly et al., 1996; Figure 1B). Assays were compared with OK107-Gal4/+ driver control and w^{1118} genetic background control 0–2 days post-eclosion (dpe), a critical period with high FMRP expression (Doll and Broadie, 2015; Doll et al., 2017; Tessier and Broadie, 2008). Representative MB Kenyon cell (KC) images and quantification are shown in Figure 1.

The MB circuit can be imaged immediately for native PKA-SPARK fluorescence (Figure 1A). PKA-SPARK reports PKA activity as round GFP puncta (Figures 1A and 1C). In control animals, PKA-SPARK puncta are largely restricted to KC somata, with few puncta in the MB calyx dendritic arbors and only rare puncta in the MB axonal lobes (Figures 1A, 1C, 2A, and 2E). To quantify PKA-SPARK activation, puncta were first counted in the KC somata and the MB calyx. A summary of the PKA-SPARK data for all of these conditions with their matched controls is shown in Figure 1. We first sought to replicate previous results with dFMRP LOF/RNAi paired with GOF/OE studies. Consistent with expectations, *dfmr1* RNAi results in a clear reduction in PKA-SPARK puncta (Figure 1D). MB-targeted RNAi results in a striking, more than 70% reduction in PKA-SPARK puncta in MB KCs compared with matched controls (normalized control, 1.0 ± 0.0466 [n = 12]; *dfmr1* RNAi, 0.294 ± 0.0282 [n = 12]; $p < 0.0001$; Figure 1I). Consistent with this, MB-targeted dFMRP OE results in a striking increase in PKA-SPARK puncta (Figure 1E). dFMRP OE results in a more than 300% increase in PKA-SPARK puncta in MB KCs compared with the matched controls (normalized control, 1.0 ± 0.0654 [n = 16]; dFMRP OE, 3.013 ± 0.2371 [n = 17]; $p < 0.0001$; Figure 1I). Given this particularly striking GOF phenotype, we hypothesized that OE of other FMRP alleles would provide insights into the molecular mechanisms of FMRP-dependent PKA activation.

We began with the FXS patient-derived R138Q point mutant *(Drosophila* R140Q; Myrick et al., 2015a). Although R140Q OE results in increased PKA-SPARK puncta in KCs (Figure 1F), the increase is modest compared with WT dFMRP OE (Figure 1E). This result could reflect reduced PKA activation or an unexpected alteration in subcellular localization of PKA activation (see below). With quantification, PKA-SPARK puncta are increased ~75% in the R140Q mutant compared with the matched transgenic controls (normalized control, 1.0 ± 0.0878 [n = 12]; R140Q OE, 1.769 ± 0.0989 [n = 12];$p< 0.0001$; Figure 1I). We next tested for a conserved effect with hFMRP. Similar to dFMRP OE, hFMRP OE results in a clear and striking increase in PKA-SPARK puncta (Figure 1G). Quantification shows an ~400% increase in PKA-SPARK puncta (normalized control, 1.0 ± 0.0356 [n = 14]; hFMRP OE, 4.221 ± 0.1691 [n = 15]; $p < 0.0001$; Figure 1I), demonstrating a strong conservation of molecular function between dFMRP and hFMRP in promoting PKA activity. Last, we tested transgenic hFMRP lacking the RNA-binding RGG box (ΔRGG). To our great surprise,

ΔRGG loss results in a particularly striking alteration of PKA-SPARK localization in MB KCs, with extensive fibrillar assemblies in somata and proximal processes (Figure 1H). Based on the penetrance and striking nature of these hFMRP-ΔRGG cytosolic fibrils, we returned to test these assemblies in extensive studies.

To confirm PKA-SPARK results, we turned to a hallmark of activated PKA-C: activation loop T197/T198 phosphorylation (Taylor et al., 2013). The PKA-C P-T198 antibody recognizes *Drosophila* phospho-PKA-C (Androschuk et al., 2018). As reported previously, we detect elevated phospho-PKA-C labeling in brain regions dorsal to the MB, specifically in MB KC somata (Androschuk et al., 2018; Figure S1A). As expected, targeted PKA-C expression selectively in the MB strongly increases the phospho-PKA-C signal (control, 1.0 ± 0.0332 [n = 13]; PKA-C OE, 1.698 ± 0.119 [n = 10]; p = 0.0002; Figures S1A and S1B). hFMRP OE also results in a significant increase in the phospho-PKA-C signal, consistent with the above PKA-SPARK results (control, 1.0 ± 0.0187 [n = 15]; hFMRP OE, 1.283 ± 0.0406 (n = 16); p < 0.0001; Figures S1A and S1B). R140Q OE results in a modest reduction in phospho-PKA-C, consistent with this reduced overall effect (control, 1.0 ± 0.02398 [n = 20]; R140Q OE, 0.8936 ± 0.03133 [n = 10]; p = 0.0141). Finally, we tested hFMRP-ΔRGG OE, predicting that PKA-SPARK would accurately report PKA activity despite the hFMRP-ΔRGG fibrillar assemblies. Consistent with this MB-targeted hFMRP-ΔRGG elevates phospho-PKA-C to mimic the PKA-SPARK result (control, 1.0 ± 0.03999 [n = 9]; ΔRGG OE, 2.1 ± 0.1313 [n = 16]; p < 0.0001; Figures S1A and S1B). These findings confirm the highly altered KC PKA activity.

We next tested whether differences in transgenic expression could explain some variant FMRP phenotypes. For example, the R140Q mutant has a reduced effect on elevated PKA-SPARK punctum number and phospho-PKA-C intensity (Figures 1 and S1). Therefore, we tested for any correlation with reduced R140Q expression while also testing for FMRP expression in other transgenic variants. To accurately assay MB differences, dissected central brain regions of stage 0–3 dpe transgenic animals were tested with western blot analyses (Figures S1C–S1F). In quantified comparisons, the R140Q levels are similar but slightly increased relative to WT dFMRP (dFMRP WT versus R140Q OE, p = 0.0523; Figures S1C and S1D), as also reported previously (Myrick et al., 2015a). These results show that differences in R140Q levels do not correlate with the decreased PKA activity. There is an interesting isoform balance difference in the R140Q mutant that could correlate with some R140Q phenotypes (see below). Despite the drastic elevation in hFMRP-ΔRGG PKA activity and fibrillar assembly localization, there is also only a modest increase in hFMRP-ΔRGG transgenic expression levels (normalized to hFMRP WT, 1.0 ± 0.03139 [n = 6]; ΔRGG OE, 1.580 ± 0.2173 [n = 6]; p = 0.0441; Figures S1E and S1F). Thus, phenotypes do not correlate with differential expression, but we also directly test the effects of reduced expression below.

dFMRP-R140Q Promotes Mislocalized PKA Activity in the MB Calyx

We next tested FMRP variants in the subcellular localization of PKA activation. We hypothesized that the modest effect of the R140Q point mutant compared with WT FMRP OE on PKA-SPARK activation (Figure 1E versus Figure 1F) could be due to (1) reduced

PKA activation, with the R140Q residue directly promoting PKA activity, or (2) altered subcellular localization of PKA activation. When assaying PKA-SPARK activation in controls, the vast majority of PKA-SPARK puncta are restricted to KC somata (Figure 1A). PKA-SPARK puncta in MB calyx dendrites, although present, occur with a much lower frequency, with reduced size and fluorescence intensity (Figure 2A). Indeed, the rarely observed activated PKA-SPARK puncta in the calyx are generally similar in intensity to low-level background fluorescence, making unequivocal resolution difficult (Figure 2A, dashed circle). In contrast, dFMRP-R140Q animals contain large activated PKA-SPARK puncta in dendritic arbors in the MB calyx (Figure 2B, dashed circle). PKA-SPARK puncta in the mutants also exhibit significantly greater fluorescence intensity than the surrounding fluorescence as well as much more intense fluorescence than control MB calyx puncta (Figure 2A versus Figure 2B). These results indicate that dFMRP R140Q mutants manifest aberrant, mislocalized PKA-SPARK activation in KC dendritic arbors, generating distinctive PKA-SPARK puncta in the MB calyx.

In quantified comparisons, dFMRP R140Q animals exhibit an ~300% increase in PKA-SPARK punctum number in the MB calyx compared with matched controls (normalized control, 1.0 ± 0.148 [n = 13]; R140Q OE, 2.99 ± 0.429 [n = 14]; p = 0.0005; Figure 2C), with a nearly 150% increase in PKA-SPARK fluorescence intensity in the MB calyx (normalized control, 1.0 ± 0.0595 [n = 13]; R140Q OE, 1.477 ± 0.0497 [n = 14]; p < 0.0001; Figure 2D). We next tested whether introduction of the R140Q mutant in a *dfmr1* -null background would promote the same mislocalized PKA activity. Similar to the OE condition, the R140Q mutant in an otherwise *dfmr1*-null background also results in strongly increased PKA-SPARK puncta in the MB calyx (Figure S2A, right panel). Indeed, quantification reveals an even greater, more than 700% increase in PKA-SPARK puncta in the MB calyx (normalized control, 1.0 ± 0.0568 [n = 9] versus R140Q; *dfmr1*, 7.821 ± 1.392 [n = 10]; p = 0.0008) compared with the consistently small punctum elevation overall (Figures S2B and S2C). This condition also exhibits a significant, ~200% increase in PKA-SPARK fluorescence intensity in the MB calyx (normalized control, 1.0 ± 0.0743 [n = 9] versus R140Q; *dfmr1*, 1.973 ± 0.175 [n = 10]; p = 0.0002; Figure S2D). Taken together, these results show that WT FMRP normally restricts most PKA activation to the KC somata in the MB circuit but that the R140Q point mutation is sufficient to drive mislocalized PKA activation within the KC dendritic arbors in the MB calyx.

Among the FMRP variants tested, R140Q mutants show striking alterations in MB circuit architecture, with reduced, shortened, or even completely missing axonal lobes (Figure 2E). In controls, robust α, α', β, β', and γ lobes project near the rostral edge of the brain (Figure 2E, top). The γ lobe is a relatively thick medial neuropil, whereas the β/β' lobes are located just caudally. The considerably thinner α/α' lobes project dorsally (Figure 2E, top). In contrast, R140Q OE axonal lobes are very reduced, with thin/absent α and α' lobes and thin γ lobes (Figure 2E, bottom). We tested whether introducing the R140Q mutant into otherwise *dfmr1* nulls also results in this aberrant MB architecture (Figure S2E). In controls (OK107-Gal4/+), the α, α', β, β', and γ MB axonal lobes show robust and consistent projections (Figure S2E, left). In the R140Q mutant in the dfmr1-null background (UAS-R140Q-dFMRP/+; $dfmr1^{50}M/dfmr1^{50}M$; OK107-Gal4/+), the α/α' and γ lobes are greatly reduced in size or missing altogether (Figure S2E, right). We finally tested whether the

Rugose PKA anchor or PKA-C levels are altered under this condition. Anti-Rugose labeling shows more puncta of reduced fluorescence intensity in R140Q mutants (control somata/surround, 1.472 ± 0.05396 [n = 10]; R140Q OE, 1.222 ± 0.06845 [n = 9]; p = 0.0114; Figures S3A and S3B). However, PKA-C localization is unaltered (Figure S3C). Together, these results show that R140Q does not affect overall PKA-C expression but does mislocalize PKA activation and strongly disrupt MB circuit architecture.

Given these severe MB defects, we hypothesized that R140Q mutants may exhibit heightened oxidative stress. To test this idea, we used a mitochondrial oxidation reporter (MitoTimer) to assay oxidative stress in KCs (Laker et al., 2014). This tool uses a RFP analog with GFP-like excitation/emission (green), which then displays RFP-like excitation/emission (red) when oxidized (Laker et al., 2014). In our imaging parameters, MB-driven MitoTimer reports an ~1:1 red:green (R:G) ratio in controls, with KC somata of low (<0.5 R:G), medium (0.5–2.0 R:G), and high (>2.0 R:G) ratios (control R:G, 0.9428 ± 0.03151 [n = 34]; Figure 2F). With R140Q mutant OE, there is a dramatic increase in the high range with an elevated R:G ratio (Figure 2F). With quantification, the overall R140Q OE mutant R:G ratio throughout the KC somata is more than 2-fold higher than that of matched transgenic controls (control R:G, 0.9428 ± 0.0315 [n = 34]; R140Q OE, 2.06 ± 0.11 [n = 31]; p < 0.0001; Figure 2G). When testing oxidative stress under the other conditions, we also drove WT dFMRP and PKA-C OE (Figure 2F). Like controls, R:G ratios are primarily in the medium R:G range in both cases (dFMRP WT OE R:G, 1.022 ± 0.0466 [n = 20]; PKA-C OE, 0.967 ± 0.039 [n = 22]; Figure 2G). Taken together, these results show that the R140Q mutation promotes oxidative stress in MB KCs, providing a mechanism for the severely disrupted MB circuit architecture.

We next tested whether reduced transgenic expression causes similar R140Q defects. With the weak 201Y-Gal4 γ-lobe driver, live imaging was more difficult than above, so we labeled PKA-SPARK (GFP tag). In controls, puncta remain largely restricted to KC somata (Figure S3D). In R140Q animals, punctum numbers are similar (normalized control, 1.0 ± 0.1220 [n = 9]; R140Q OE, 1.342 ± 0.1953 [n = 10]; p = 0.158; Figure S3E) but significantly more intense (control, 1.0 ± 0.0252 [n = 9]; R140Q OE, 1.263 ± 0.0426 [n = 10]; p < 0.0001; Figure S3F). This suggests expression effects on KC somata compared with MB calyx PKA activity, with higher levels required to produce PKA-SPARK puncta in the calyx. Gal4 function is reduced at low temperature (Duffy, 2002), so we next tested animals reared at 18°C. Similar to the above results (25°C), controls exhibit PKA-SPARK puncta only in KC somata, whereas R140Q results in high punctum numbers in the calyx (normalized control, 1.0 ± 0.1344 [n = 9]; R140Q OE, 7.771 ± 0.4377 [n = 11]; p < 0.0001; Figures S3G and S3I). Overall punctum numbers are similar (normalized control, 1.0 ± 0.0925 [n = 9]; R140Q OE, 1.072 ± 0.0461 [n = 11]; p = 0.1308; Figure S3H). Like above, calyx PKA-SPARK puncta are significantly more intense in R140Q OE animals (Figures S3G and S3J). MB lobe defects persist at 18°C, albeit with reduced severity, and α/α' lobes remain disrupted (Figure S3K). Taken together, these results suggest that the R140Q mutation promotes increased PKA activity, with localized higher levels of PKA activation in the MB calyx.

Transgenic hFMRP and Elevated PKA Activity Repress dFMRP Expression

Biochemical studies indicate that FMRP binds its own mRNA, suggesting a feedback loop of direct negative self-regulation (Blice-Baum and Mihailescu, 2014; Schaeffer et al., 2001). *Drosophila* provides an opportunity to test this hypothesis *in vivo*, with the prediction that evolutionarily conserved hFMRP (Coffee et al., 2010) should repress dFMRP expression levels. In controls, dFMRP levels in MB KCs are similar to surrounding brain somata, with only a slight trend of increased MB levels (Figures 3A and 3F). With MB-targeted hFMRP OE, dFMRP is reduced by ~50% compared with controls (normalized control, 1.0 ± 0.042 [n = 14]; 0.494 ± 0.0194 [n = 18]; $p < 0.0001$; Figures 3B and 3D). Consistent with targeted hFMRP OE producing a cell-autonomous effect, dFMRP levels in the surrounding brain remain unaffected (normalized control, 1.0 ± 0.0555 [n = 14]; hFMRP OE, 0.953 ± 0.048 [n = 18]; $p = 0.887$; Figures 3B and 3E). This difference is also reflected in the ratio between dFMRP levels in the MB compared with the surrounding brain regions (control, 1.129 ± 0.0394 [n = 14]; hFMRP OE, 0.586 ± 0.0198 [n = 18]; $p < 0.0001$; Figure 3F). We therefore conclude that dFMRP levels are reduced significantly with targeted transgenic hFMRP in the MB, demonstrating that hFMRP is sufficient to restrict dFMRP levels *in vivo*. These results strongly suggest that FMRP suppresses its own expression in the brain learning and memory circuitry.

We next tested the hypothesis that PKA activity suppresses FMRP via a negative feedback loop. To test this idea, PKA-C OE was targeted to the MB circuit (Kiger et al., 1999). PKA-C OE causes a strong decrease in dFMRP in KCs (Figure 3C). With quantification, PKA-C OE causes an ~35% reduction in FMRP levels compared with controls (normalized PKA-C OE, 0.656 ± 0.0332 [n = 12]; $p < 0.0001$; Figure 3D), whereas FMRP expression in surrounding cells is unaltered (normalized PKA-C OE, 0.9743 ± 0.0398 [n = 12]; $p = 0.9742$; Figure 3E), and the FMRP ratio in MB compared with surrounding cells is reduced (PKA-C OE, 0.751 ± 0.0318 [n = 12]; $p < 0.0001$; Figure 3F). Testing whether similar results occur without PKA-SPARK, we find that MB-targeted hFMRP and PKA-C still reduce dFMRP levels (Figures S4A and S4C). hFMRP OE (control, 1.042 ± 0.0164 [n = 22]; hFMRP OE, 0.625 ± 0.0147 [n = 23]; $p < 0.0001$; Figure S4B) and PKA-C OE (control ratio, 0.991 ± 0.0207 [n = 9]; PKA-C OE, 0.628 ± 0.0207 [n = 9]; $p < 0.0001$; Figure S4D) result in significantly reduced dFMRP. Western blot tests of dFMRP levels show a trending reduction with hFMRP OE (control, 1.0 ± 0.145; hFMRP OE, 0.7187 ± 0.141) but no other changes (Figures S4E and S4F). Together, these results indicate that hFMRP represses dFMRP and that PKA activity also represses FMRP levels, arguing for an FMRP-PKA negative feedback mechanism controlling FMRP in the MB circuit.

The above dFMRP experiments used anti-GFP labeling to assay PKA-SPARK. Given potential antibody versus native GFP imaging differences, we quantified PKA-SPARK puncta in these preparations in the same way. If consistent observations and quantified comparisons occur in antibody-labeled preparations, then fixation must preserve the integrity of the *in vivo* PKA-SPARK biosensor. Compared with controls, hFMRP OE animals display greatly increased PKA-SPARK puncta in KCs (Figures 3A and 3B). Quantification demonstrates a more than 400% increase in PKA-SPARK punctum number (normalized control, 1.0 ± 0.087 [n = 14]; hFMRP OE, 4.226 ± 0.2345 [n = 18]; $p < 0.0001$). Like native

PKA-SPARK GFP imaging, MB calyx puncta remain infrequent in controls and hFMRP OE animals but are clearly elevated with dFMRP-R140Q OE. Consistent with the above results, PKA-C OE also drives activated PKA-SPARK localization in very large, highly fluorescent puncta in antibody-labeled preparations (Figure 3C). We also tested hFMRP localization in this context, finding that MB-driven hFMRP localizes broadly in the cytoplasm while also displaying bright round punctate localization (Figure S4G). Interestingly, hFMRP antibody labeling also surrounds many of the PKA-SPARK puncta (Figure S4G, arrows). Taking these results together, we conclude that fixed antibody labeling preserves native GFP fluorescence PKA-SPARK subcellular localization and reporter activity.

To test the PKA activity-dependent increase in PKA-SPARK, we next assayed loss of *rutabaga (rut)* adenylyl cyclase (Lee, 2015), which produces cAMP to activate PKA (Halls and Cooper, 2017). In the MB, *rut* is necessary for learning and memory (Zars et al., 2000). We therefore hypothesized that *rut* loss would suppress MB PKA-SPARK activation from hFMRP OE. To test this idea, we used characterized UAS-rut RNAi (Wang et al., 2020; BDSC 27035), MB-targeted with OK107-Gal4, alone and with hFMRP OE (Figure S4H). KC labeling done as above compared the transgenic control (top left), *rut* RNAi (top right), hFMRP OE (bottom left), and hFMRP OE combined with *rut* RNAi (bottom right). MB-targeted *rut* RNAi strongly reduces PKA-SPARK puncta (Figure S4H). In quantified comparisons, *rut* RNAi reduces PKA-SPARK by more than 50% (normalized control, 1.0 ± 0.0759 [n = 13]; *rut* RNAi, 0.4993 ± 0.0498 [n = 11]; p = 0.0001; Figure S4I). This result shows reduced PKA activation with the PKA-SPARK reporter. As above, hFMRP OE strongly increases PKA-SPARK puncta (Figure S4H). Quantification shows a more than 400% increase (hFMRP OE, 4.071 ± 0.207 [n = 8]; p < 0.0001; Figure S4I). This hFMRP elevation is suppressed to control levels by *rut* RNAi (Figure S4H). Quantification shows that *rut* RNAi completely eliminates the hFMRP OE elevation (hFMRP OE, *rut* RNAi, 0.9273 ± 0.077 [n = 20]; p = 0.983; Figure S4I). Taken together, these results again confirm the PKA-SPARK activity reporter and that hFMRP promotes PKA activation.

hFMRP-ΔRGG Colocalizing with PKA-SPARK in Fibrillar Assemblies Represses dFMRP

The most surprising result from the PKA-SPARK screen was hFMRP-ΔRGG, with the normal small, round activated puncta in controls (Figure 1C) replaced with long, fibrillar assemblies in mutants (Figure 1H). This striking transformation could reflect a change in FMRP function. To test this idea, hFMRP-ΔRGG animals were labeled for dFMRP to show a striking dFMRP decrease in KCs with PKA-SPARK present (Figures 4A–4D) and absent (Figures S5A and S5B). Quantitatively, hFMRP-ΔRGG causes an ~40% reduction in dFMRP levels (normalized control, 1.0 ± 0.0442 [n = 13]; ΔRGG OE, 0.594 ± 0.024 [n = 13]; p < 0.0001; Figure 4C) and an ~30% reduction in the KC/surrounding brain tissue dFMRP intensity ratio (control, 1.028 ± 0.0258 [n = 13]; ΔRGG OE, −0.723 ± 0.0285 [n = 13]; p < 0.0001; Figure 4D), with unaltered dFMRP levels in the brain regions where hFMRPΔRGG is not targeted (control, 1.0 ± 0.0534 [n = 13]; ΔRGG OE, 0.8589 ± 0.055 (n = 13); p = 0.0781). Consistent with this, hFMRP-ΔRGG OE without PKA-SPARK also results in reduced dFMRP intensity ratios (control, 1.004 ± 0.0216 [n = 14]; ΔRGG OE, 0.8293 ± 0.0229 [n = 13]; p < 0.0001; Figures S5A and S5B). We conclude that, despite the altered activated PKA-SPARK localization, hFMRP-ΔRGG retains the ability to suppress

dFMRP expression. Given the striking PKA-SPARK fibrillar assemblies with hFMRP-ΔRGG OE, the subcellular localization was next examined in more detail.

With hFMRP-ΔRGG OE, a single elongated PKA-SPARK fibrillar assembly coils within the KC soma (Figure 4E, right panel), often entering proximal process (Figure S5C, arrows). z stacks reveal a tangled mass of PKA-SPARK assemblies throughout the MB (Figure S5C; Video S1). Single confocal slices were used to measure the length (long axis) and width (short axis) of assemblies in single cells. hFMRP-ΔRGG OE causes a huge increase in length (control long axis, 0.8863 ± 0.0433 μm [n = 40]; ΔRGG OE long axis, 5.413 ± 0.4563 μm [n = 30]; $p < 0.0001$; Figures 4E and 4F). A weaker driver (201Y-Gal4) similarly displays activated PKA-SPARK fibrillar assemblies, albeit shorter compared with OK107-Gal4 and primarily restricted to cell bodies (201Y-Gal4 ΔRGG OE long axis, 2.624 ± 0.0494 [n = 803]; $p < 0.0001$; Figures S5D and S5E). As another control, we also tested the ERK-SPARK reporter (Zhang et al., 2018). ERK-SPARK puncta are observed in KC somata (Figure S6A), with no puncta present in the unphosphorylatable control (Figure S6B). Importantly, there is no change in the ERK-SPARK reporter with hFMRP-ΔRGG OE, and no fibrillar assemblies are observed (Figures S6A–S6D). Given the PKA-SPARK reporter specificity and phospho-PKA-C confirmation, we conclude that hFMRP-ΔRGG OE promotes mislocalized, greatly elevated PKA activation in MB KC somata and proximal processes.

Despite reduced expression levels, dFMRP localization appears to be unchanged by hFMRP-ΔRGG OE compared with controls, with broad cytosolic labeling in KCs (Figures 4G and 4H, magenta). Because the PKA-SPARK reporter is also cytosolic, co-expression results in co-occurrence with weak correlation between dFMRP and hFMRP-ΔRGG localization (MCC1:MCC2 above autothreshold, 0.720:0.677; PCC without autothreshold, 0.43; PCC with autothreshold, 0.18; Figure 4H). We hypothesized that hFMRP-ΔRGG co-localization with PKA-SPARK assemblies would indicate that hFMRP-ΔRGG is localizing PKA activity along with subcellular distribution. Consistent with this, hFMRP-ΔRGG and PKA-SPARK co-labeling shows co-localization along extensive fibrillar assemblies (Figure 4I). Quantitatively, there is a high degree of co-occurrence and overlap correlation (MCC1:MCC2 above autothreshold, 0.816:0.804; PCC without autothreshold, 0.65; PCC with autothreshold, 0.56; Figure 4I). Similarly, 201Y-Gal4 driving hFMRP-ΔRGG results in co-localization in activated PKA-SPARK assemblies (Figure S5F). We therefore next tested whether dFMRP is required for hFMRP-ΔRGG/PKA-SPARK assembly. MB-targeted hFMRP-ΔRGG OE in otherwise *dfmr1*-null mutants results in similar elongated, fibrillar PKA-SPARK assemblies (Figures S7A and S7B). This result indicates that hFMRP-ΔRGG is sufficient to promote mislocalized PKA activation with subsequent generation of extensive PKA-SPARK assemblies.

The most common brain hFMRP isoform (7) is identical to the longest hFMRP, except for lacking a 17-amino acid segment within the LC domain (Figure 1B; Ramos et al., 2006). To test whether this domain is required for localized PKA activation and fibrillar assembly formation, we next employed FL hFMRP with an intact LC domain (Coffee et al., 2010). Like isoform 7, hFMRP FL increases PKA-SPARK puncta with fluorescently intense round punctate localization (Figure S7C). Although most activated PKA-SPARK in is round

puncta, there are occasional short fibrils, suggesting a limited capacity to form fibrillar assemblies (Figure S7C, arrow). Under these conditions, hFMRP-ΔRGG OE produces much more extensive assemblies. Comparable with WT hFMRP and hFMRP-ΔRGG OE, hFMRP FL OE also strongly reduces dFMRP levels (normalized to surrounding intensity, 1.0 ± 0.0339 [n = 6]; KC, 0.6403 ± 0.02654 [n = 6]; $p < 0.0001$; Figures S7D and S7E). Because the only difference between hFMRP-ΔRGG and hFMRP FL is the absence of the RGG box, and because hFMRP-ΔRGG forms assemblies over a short period of time and at lower protein levels (see below), these findings confirm that the RGG box is required to suppress the fibrillar phenotype. Together, these results demonstrate that the RGG/LC region is required to prevent formation of the cytosolic fibrillar assemblies, driving PKA activity in a similar localized pattern.

hFMRP-ΔRGG Colocalizes with Markers for Ribonucleoprotein (RNP) and Cytosolic Fibrillar Aggregation

To assess aberrant hFMRP-ΔRGG localization, we tested subcellular distribution with membrane, nuclear, and organelle markers. Importantly, even without PKA-SPARK present, hFMRP-ΔRGG forms fibrillar assemblies in KCs (Figures 5A–5E, magenta). Double labeling with the neuronal membrane marker anti-horseradish peroxidase (HRP) shows hFMRP-ΔRGG in the membrane-adjacent cortex (Figure 5A). Quantitatively, there is low co-occurrence and correlation (MCC1:MCC2 above autothreshold, 0.176:0.301; PCC without autothreshold, 0.15; PCC above autothreshold, −0.39; Figure 5F). With SYTO nuclear labeling, hFMRP-ΔRGG is outside of the nucleus (Figure 5B). Quantitatively, there is again low co-occurrence and correlation (MCC1:MCC2 with autothreshold, 0.001:1.0; PCC without autothreshold, −0.25; PCC with autothreshold, −0.25; Figure 5F). Rugose and hFMRP-ΔRGG also show low co-occurrence and correlation (MCC1:MCC2 with autothreshold, 0.591:0.421; PCC without autothreshold, 0.21; PCC with autothreshold, −0.13; Figures 5C and 5F). FMRP and Staufen colocalize in RNP processing bodies (Barbee et al., 2006), so anti-Staufen was tested (St Johnston et al., 1991). Double labeling shows tight co-localization, with long stretches of co-labeled hFMRP-ΔRGG/Staufen fibrillation (Figure 5D, arrows). Quantitatively, there is high co-occurrence and correlation with Staufen (MCC1:MCC2 with autothreshold, 0.711:0.607; PCC without autothreshold, 0.56; PCC with autothreshold, 0.37; Figure 5F). These results show that hFMRP-ΔRGG and activated PKA-SPARK colocalize with Staufen in fibrillar cytosolic assemblies together with RNP processing bodies or as a consequence of processing body activity.

Given the continuous, elongated hFMRP-ΔRGG/PKA-SPARK assemblies in the MB KCs, we hypothesized that they represent cytosolic fibrillar protein aggregates (Kim et al., 2013; Molliex et al., 2015). To test for fibrillar aggregation, we employed the well-documented protein aggregation marker thioflavin T (ThT), which undergoes a strong redshift in spectral excitation and emission when bound to fibrillar aggregates (Kim et al., 2013; Nil et al., 2019). The hFMRP-ΔRGG OE condition shows colocalization between the ThT marker and hFMRP-ΔRGG in the MB KCs (Figure 5E). However, analyses were complicated by ThT nuclear labeling. As a consequence, initial quantification showed modest co-occurrence and localization correlation (MCC1:MCC2 with autothreshold, 0.286:0.523; PCC without autothreshold, 0.28, PCC with autothreshold, −0.15). Therefore, neuronal nuclei were

colabeled with the nuclear marker DRAQ5 and the nuclei were subtracted from confocal images prior to analyses. With this nuclear subtraction, there is both high co-occurrence and strong correlation between the ThT marker and hFMRP-ΔRGG (MCC1:MCC2 with autothreshold, 0.333:0.430; PCC without threshold, 0.72, PCC with autothreshold, −0.18; Figure 5F, bottom). Taken together, these results are consistent with the conclusion that activated PKA-SPARK, hFMRP-ΔRGG, and Staufen colocalize together into cytosolic fibrillar aggregates in MB KCs.

hFMRP-ΔRGG Promotes Spherical Aggregates before Forming Elongated Assemblies

Drosophila cell culture work suggests that loss of the RGG domain interferes with subcellular localization with reduced intracellular shuttling (Gareau et al., 2013a, 2013b). Given that processing bodies result from liquid-phase transition states of particles containing LC protein sequences (Luo et al., 2018), we next pursued a range of assays to test the composition, dynamics, and stability of the cytosolic fibrillar hFMRP-ΔRGG/ PKA-SPARK assemblies in MB KCs. In WT controls, PKA phosphorylation activated PKA-SPARK appears as small, round fluorescent puncta, so we hypothesized that early activated hFMRP-ΔRGG aggregates begin with this simple spherical morphology before stabilizing into the elongated, fibrillar assemblies. To test the dynamics of hFMRP-ΔRGG/PKA-SPARK assembly, we used temperature-sensitive Gal80 ($Gal80^{ts}$) to temporally regulate transgenic Gal4-mediated expression in MB KCs (McGuire et al., 2003). At the permissive low temperature (18°C), $Gal80^{ts}$ is functional as a transcriptional repressor and prevents Gal4 from driving expression of hFMRP-ΔRGG. At the restrictive high temperature (32°C), $Gal80^{ts}$ is no longer functional as a transcriptional repressor, and OK107-Gal4 drives hFMRP-ΔRGG expression. $Gal80^{ts}$ was used to regulate transgenic expression in MBs KCs over a short period (overnight [O/N], ~16 h) and long period (~7 days) to test the dynamics of hFMRP-ΔRGG/PKA-SPARK assembly formation. Representative images of both time periods are shown in Figure 6.

With short induction, MB KCs expressing hFMRP-ΔRGG display activated PKA-SPARK puncta with higher fluorescence than controls as well as more weakly fluorescent, short but elongated fibrillar assemblies (Figure 6A). This presentation is reminiscent of the weaker, more restricted MB 201Y-Gal4 driver line detailed above. Quantification of these PKA-SPARK assemblies reveals limited formation of elongated fibrils (long axis length, 2.795 ± 0.03333 μm; n = 937). Double labeling shows that overlap between PKA-SPARK puncta and hFMRP-ΔRGG occurs but is limited, with instances of hFMRP-ΔRGG surrounding spherical PKA-SPARK puncta (Figure 6C). In most cases, hFMRP-ΔRGG is widely distributed in the cytosol of MB KC somata (Figure 6C, bottom center panel; compare with Figure 4I, center panel). With long induction, larger, more highly fluorescent PKA-SPARK puncta occur, with a striking increase in elongated, fibrillar assemblies (Figure 6B). Quantitatively, PKA-SPARK assemblies, after 1 week of induction, are very significantly more elongated (long axis length, 4.561 ± 0.05565 μm [n = 1,283]; $p < 0.0001$ compared with O/N; Figure 6B). Double labeling shows strong overlap of hFMRP-ΔRGG with these fibrillar PKA-SPARK assemblies (Figure 6D, bottom panels, arrows). Moreover, intense hFMRP-ΔRGG labeling now clearly surrounds the large activated PKA-SPARK puncta (Figure 6D, arrowheads). Taken together, these results show that hFMRP-ΔRGG promotes

formation of large PKA-SPARK puncta before colocalizing together into the elongated, fibrillar assemblies. This assembly process is reminiscent of reports of LC domain dynamics *in vitro*.

hFMRP-ΔRGG/PKA-SPARK Assemblies Form Because of LC Domain Aggregation

Cell culture studies of FMRP lacking the RGG domain show disruption of normal liquid-liquid phase separation (Mazroui et al., 2002). LC domains occur adjacent to the RGG box, and FMRP LC domains self-assemble into highly ordered, densely packed, gel-like, phase-separated aggregates *in vitro* (Kato et al., 2012). Importantly, LC aggregation is temperature sensitive and labile, with rapid dispersion at elevated temperature (Molliex et al., 2015). We hypothesized that LC aggregation may drive hFMRP-ΔRGG/PKA-SPARK assembly *in vivo*. Live PKA-SPARK imaging in MB KCs allows direct assays of assembly dynamics and aggregation/de-aggregation kinetics with acute temperature shifts. We tested whether short bouts of elevated temperature reverse hFMRP-ΔRGG/PKA-SPARK assembly in MB KCs. Acutely dissected brains were live imaged before and after 20-min incubation at various temperatures. At 25°C, PKA-SPARK distribution in hFMRP-ΔRGG animals is unaltered (Figure 7A, top). At 42°C, however, PKA-SPARK fibrillar assemblies at t = 0 are replaced with small, spherical puncta with concurrent loss of elongated assemblies (Figure 7A, bottom). With shorter 10-min temperature regimens, MB KCs display highly colocalized hFMRP-ΔRGG and PKA-SPARK after 25°C (Figure 7B, top), but hFMRP-ΔRGG is much more diffuse, with hFMRP-ΔRGG surrounding the newly emergent PKA-SPARK puncta after 42°C (Figures 7B, bottom, and 7C, arrows). The threshold for assembly de-aggregation is ~41°C for 10–20 min, with the elongated hFMRP-ΔRGG/PKA-SPARK fibrillar assemblies replaced with the appearance of spherical puncta.

As a final test of the activated PKA-SPARK assembly dynamics, we imaged live disassembly/assembly during and after an acute temperature shift (Figure 7D; Video S2). The main objective was to determine whether emergent activated PKA-SPARK puncta occur independently or arise from disassembly of pre-existing elongated fibrillar assemblies. To test these two alternatives, the elevated temperature shift was applied remotely to acutely dissected isolated brains while continuously imaging with time-lapse confocal microscopy (Figure 7D; Video S2). During the temperature elevation, elongated PKA-SPARK assemblies in MB KCs rapidly shrink down into spherical puncta, showing that the puncta emerge from the elongated fibrils as a consequence of simultaneous assembly de-aggregation (Figure 7D; Video S2). Consistent with this observable disaggregation, the dispersed PKA-SPARK GFP fluorescence increases rapidly, demonstrating that the disaggregated reporter quickly expands into the neuronal cytosolic space. These results indicate that PKA-SPARK puncta arise from pre-existing PKA-SPARK assemblies or, at a minimum, at the same subcellular locations as the fibrillar assemblies. Following the temperature shift, the elongated fibrils begin to rapidly reassemble (Figure 7D; Video S2), indicating a bidirectional process. We conclude that PKA-SPARK fibrils have opposing dynamic assembly and disassembly processes, with hFMRP-ΔRGG-dependent PKA activation driving early punctum formation and hFMRP-ΔRGG recruitment resulting in later gross mislocalization into the elongated cytosolic assemblies. Together, these results suggest that the FMRP RNA-binding RGG box regulates partitioning into LC domains.

DISCUSSION

In FXS models and patient-derived cells, FMRP promotes induction of the PKA activator cAMP (Berry-Kravis and Huttenlocher, 1992; Berry-Kravis et al., 1995; Kelley et al., 2007). Consistent with this, we find PKA activation with multiple variant *Drosophila* and human FMRPs. We show that PKA activation (PKA-C OE) represses *Drosophila* FMRP in KCs, indicating FMRP-PKA signaling negative feedback. Human FMRP, with or without the RNA-binding RGG domain, represses *Drosophila* FMRP in KCs. FMRP binds its own mRNA (Blice-Baum and Mihailescu, 2014; Schaeffer et al., 2001) and canonically suppresses translation of bound transcripts (Darnell et al., 2011). These results suggest FMRP-FMRP and PKA-FMRP negative feedback loops. Control mechanisms may depend on RNA-level regulation or protein-protein interactions. The disease-associated R140Q point mutation imbalances PKA regulation and causes oxidative stress in KCs. Loss of the RNA-binding RGG domain drives PKA partitioning and formation of cytosolic fibrillar assemblies. Based on this study, we conclude that FMRP has evolutionarily conserved roles in a bidirectional PKA activity negative feedback loop, in PKA anchor regulation, and in tight self-regulation in brain learning/memory circuitry.

The R140Q mutation mislocalizes PKA activity in KCs, indicating a key FMRP role in subcellular PKA activation. The FMRP point mutant still binds mRNA and polyribosomes but fails to enable correct synaptic architecture at the neuromuscular junction, showing mRNA binding-independent MB calyx functions (Myrick et al., 2015a). Likewise, we find an FMRP mRNA binding-independent role regulating PKA activity localization in the brain. The dFMRP-R140Q-induced increase in the PKA-SPARK activity reporter is reduced in KC somata relative to WT FMRP OE, but PKA activation in dendritic arbors is strikingly elevated. These findings are also consistent with the known effects of inappropriate and mislocalized kinase activity driving protein phosphorylation to cause circuit connectivity defects (Kang and Woo, 2019; Lanuza et al., 2019). Mislocalized hyperphosphorylation is disease linked in numerous neurological conditions (Lee et al., 2001; Yeboah et al., 2019). Thus, this patient-derived FMRP point mutant links mislocalized PKA activation and neural circuit connectivity defects in the FXS disease condition.

Human FMRP-ΔRGG promotes activated PKA-SPARK spherical puncta prior to forming long fibrillar assemblies. hFMRP-ΔRGG/PKA-SPARK assemblies disassociate with temperature, suggesting possible liquid phase separation (Molliex et al., 2015). Work with the FMRP RGG-adjacent LC region demonstrates that this domain is sufficient for phase separation (Kato et al., 2012). Similar LC domains of other proteins drives temperature-dependent phase separation (Molliex et al., 2015). It has been suggested that the RGG box and adjacent LC domains bind mRNA to promote phase separation (Weber and Brang wynne, 2012). Given the striking hFMRP-ΔRGG fibrillar assemblies, the RGG box may be involved in this process. Alternatively, FMRP aggregation may overwhelm chaperones, although hFMRP-ΔRGG fibrils appear to be quite distinct from stress granules (Mateju et al., 2017). Moreover, lowered expression and shortened induction demonstrate that hFMRP-ΔRGG assemblies are not caused by simple OE. We conclude that FMRP acts not only to drive PKA activity but also to regulate partitioning of PKA activity localization. Because

FMRP and PKA are activity-dependent regulators in learning/memory circuitry, we suggest that they together regulate mRNAs in an activity-dependent mechanism.

PKA subunits can differentially localize between processing bodies and other subcellular compartments (Tudisca et al., 2010). Our results indicate that hFMRP-ΔRGG assemblies contain processing bodies that also partition via phase separation (Luo et al., 2018). Whether phase separation is involved remains to be determined, but given PKA activity mislocalization, we predict that aberrant PKA signaling causes FXS symptoms. We show that hFMRP-ΔRGG colocalizes with Staufen, which is associated with processing bodies (Lin et al., 2008), sites of RNA regulation (Brengues et al., 2005). Consistent with this, cell culture studies also indicate Staufen/FMRP colocalization (Barbee et al., 2006). Our results also show hFMRP-ΔRGG colocalizes with the aggregation marker ThT (Kim et al., 2013; Nil et al., 2019), consistent with separation into fibrillar assemblies. Given the striking PKA activity alterations, we suggest an FMRP-PKA feedforward interaction, with hFMRP-ΔRGG mislocalizing PKA activity to promote fibrillation. Alternatively, PKA may repress fibrillation, albeit ineffectively given the assemblies formed in KCs. For example, yeast PKA phosphorylation of Pat1 prevents processing body formation (Ramachandran et al., 2011). Similarly, hFMRP-ΔRGG could be preventing PKA from normally phosphorylating targets that counteract partitioning.

Human FMRP-ΔRGG strongly suppresses dFMRP levels in KCs despite drastically altered subcellular localization. This indicates that the RNA-binding RGG box is dispensable for selfregulation. Indeed, the RGG box is not required for association with polysomal RNPs (Mazroui et al., 2003). Although FMRP binds its own transcript *in vitro* (Blice-Baum and Mihailescu, 2014; Schaeffer et al., 2001), so far there are no *in vivo* studies. Importantly, hFMRP-ΔRGG also shows temperature-dependent disassociation. In cell culture, ΔRGG causes reduced stress granule localization and intracellular shuttling (Gareau et al., 2013a, 2013b), suggesting an FMRP role in partitioned LC assembly (Kato et al., 2012). Our *in vivo* study indicates a larger role of LC assemblies. Short hFMRP-ΔRGG induction drives assembly, consistent with hFMRP-ΔRGG localization in culture studies (Mazroui et al., 2002, 2003). Although RGG/LC domains in other proteins influence aggregation dynamics, RGG/LC domain requirements during phase separation remain unclear (Alberti et al., 2019; Chong et al., 2018). Our results suggest that FMRP segregation is prevented by the RGG box via dynamic partitioning regulation, with RNA binding subcellular specificity for cytosolic compartments. Future work will test LC and RGG box separately to assay the phase separation of PKA signaling.

In conclusion, dFMRP and hFMRP have a conserved function driving PKA activity, with an mRNA binding-independent role in PKA activity localization and an mRNA binding-dependent role in restraining PKA activity. Our results also establish an RGG box-independent FMRP self-repression mechanism and FMRP-PKA bidirectional feedback loop. PKA activity localization is dependent on separable FMRP domains that determine subcellular localization, soma versus dendrites (R140Q), and in distinct cytosolic compartments (ΔRGG). The R140Q point mutant and ΔRGG domain deletion have overlapping effects on altering PKA activation, even when FMRP is otherwise absent. The correlation between FMRP levels, PKA activation, assembly dynamics, and defective MB

circuit architecture suggests a pathway. Indeed, several neural cytosolic aggregation diseases are linked to “prion-like” domain mutations (Ling et al., 2013). Future studies will focus on PKA regulation in these disease models, using neural circuits with larger somata. In the future, we will focus on FMRP as an aggregation-inducing/regulating protein that contributes to (or counteracts) progression of cellular assemblies in FXS and FXS-associated disorders. We believe that this PKA-regulating FMRP function is a mechanism key to understanding these devastating disease states.

STAR★METHODS

RESOURCE AVAILABILITY

Lead Contact—Further information and requests for resources and reagents should be directed to the lead contact, Kendal Broadie (kendal.broadie@vanderbilt.edu).

Materials Availability—Generated *Drosophila* hFMRP lines are available without restriction.

Data and Code Availability—The data that support the findings of this study are available from the corresponding authors upon request. The RatioMetric Analysis Macro is available at: https://github.com/JamesCSears/RatioMetric-Analysis-Macro-ImageJ.

EXPERIMENTAL MODEL AND SUBJECT DETAILS

Animals were maintained on standard *Drosophila* food in a 12-hour light:dark cycling incubator at 25°C. For Gal80^{ts} experiments, animals were raised at 18°C until pupal day 4 (P4), then shifted to 32°C overnight or for 7 days. Animals were staged to 0–9 days post-eclosion (PDE), with analyses done at 0–2 PDE except where noted. The genetic background w^{1118} (BDSC 3605) and RNAi background (P{y[+t7.7] = CaryP}attP2; BDSC 36303) outcrossed to Gal4 lines were used as controls. Gal4 drivers used included: OK107-Gal4 (BDSC 854) and 201Y-Gal4 (BDSC 4440). UAS responder lines used included: UAS-PKA-SPARK (Zhang et al., 2018), UAS-PKA-C^{wt} (BDSC 35555), UAS-*dfmr1*^{WT} (Myrick et al., 2015a), UAS-*rutabaga* RNAi (BDSC 27035), UAS-MitoTimer (BDSC 57323; Laker et al., 2014), *UAS-dfmr1* RNAi (BDSC 27484; Doll and Broadie, 2015, 2016), *UAS-dfmr1*^{R140Q} (Myrick et al., 2015a), *UAS-hFMRP*^{iso7} (UAS-hFMRP^{WT}; this study), *dfmr1*^{50M}, UAS-MYC-*hFMR1*^{FL} (Coffee et al., 2010) and UAS-MYC-*hFMR1*$^{\Delta RGG}$ (Coffee, 2011). For transgenic a *dfmr1* LOF studies, the *dfmr1*^{50M} null allele was used (Zhang et al., 2001). Recombination and multi-allele crossing schemes were done using standard genetic techniques.

METHOD DETAILS

PKA-SPARK Imaging—Imaging was performed as in Sears et al., 2019, with the few below modifications. Briefly; Staged adult brains were acutely dissected in 1X PBS and placed between two #1 coverslips separated by one or two layers of precut Oracal 651 matte black vinyl spacers. Separation of phases-based activity reporter of kinase (PKA-SPARK; Zhang et al., 2018) fluorescence was live-imaged for native GFP fluorescence within 10 minutes. With the exception of the live kinetic experiments, which were mounted in 1X

PBS, all brains were mounted in Fluoromount G (EMS17984). PKA-SPARK puncta number and intensity were scored slice by slice within Mushroom Body (MB) Kenyon Cell Z stacks, using the Find Maxima feature in ImageJ with the identical noise toleration settings between all compared groups.

PKA-SPARK Kinetics—For all timed temperature-dependent effects on PKA-SPARK, acutely dissected adult brains were mounted and live imaged immediately. All the preparations were then either 1) placed at 42°C on a Dri-Bath hot plate or 2) kept at RT for 20 minutes, followed by repeat re-imaging. For labeled preparations, acutely dissected brains were placed in PCR tubes and heated at the described temperatures and durations using PCR controls, then immediately fixed. For time-lapse imaging of PKA-SPARK dynamics during temperature-sensitive studies of acutely dissected brains, focus was manually maintained with heat remotely applied after the first image for the following five minutes, followed by an additional 10 minutes of imaging.

MitoTimer Imaging—Live, acutely dissected brains were mounted onto slides separated by Oracal 651 matte black vinyl spacers. Laser capture settings (488 and 543) were calibrated to control samples for a Mitotimer 1:1 red/green ratio (R:G; Laker et al., 2014). Green pixel values were the reference above background for comparison. To assess pixel-by-pixel ratiometry, the ImageJ macro Internal Coverage (Sears and Broihier, 2016) was modified to measure green pixel values above a given value, then provide in list form R:G values. This macro also assigned pixel values to set ratio ranges (< 0.5, 0.5–1,1–2 and > 2). This macro is available at https://github.com/JamesCSears/ RatioMetric-Analysis-Macro-ImageJ.

Western Blots—Studies were done as previously reported (Sears et al., 2019; Vita and Broadie, 2017; Zhang et al., 2001). Briefly; 0–3 dpe central brains were dissected in 1 X PBS containing Roche complete EDTA-free protease inhibitor (Roche: 04693159001), and then snap-frozen on dry ice. Samples (2 brains/tube) were diluted 1:1 in RIPA buffer (Sigma-Aldrich: R0278) containing phosphatase and protease inhibitors (Abcam: ab201119), then homogenized on ice. Lysates were spun (16,000 X g) for 10 mins at 4°C, LDS (Invitrogen: NP0007) and NuPAGE reducing agent added (Invitrogen: NP0009), and the samples then heated for 10 mins at 70°C. Equal volumes of lysates were loaded per lane onto a 4%−12% Bis-Tris gel (Invitrogen: NP0336), along with Full Range Rainbow MW ladder (RPN800E), with MOPS running buffer (Invitrogen: NP0001) and NuPAGE antioxidant (Invitrogen: NP0005) in the upper buffer chamber. Gels were run for 10 mins at 100V, then moved to 175–200 V. Separated proteins were transferred to nitrocellulose membranes for 1 hr 20 mins at 32V, with 10% methanol in NuPAGE transfer buffer (Invitrogen: NP0006–1) and NuPAGE antioxidant. Membranes were blocked in 2% powdered skim milk in TBS-T for 1 hr, then incubated with primary antibodies overnight at 4°C or 2.5 hr RT. Primary antibodies used were: mouse anti-dFMRP (1:1500 or 1:750; Abcam: ab10299), mouse anti-hFMRP (1:3000; Chemicon International: MAB2160) and rabbit anti-α-tubulin (1:40,000; Abcam: ab52866). Membranes were then incubated with secondary antibodies at 1:10000 for 1 hr at RT, Secondary antibodies used were: Alexa Fluor 700 goat anti-rabbit (Invitrogen: A-21038) and DyLight800 (Invitrogen: SA535521).

Membranes were imaged using a LI-COR Odyssey CLx. Protein bands were standardized to loading control (α-tubulin).

Immunocytochemistry Imaging—Staged brains were fixed in 4% paraformaldehyde in 1X PBS in 4% sucrose for 30 mins with rotation in all cases, except for anti-Staufen, SYTO Select, DRAQ5 and anti-HRP labeling, in which brains were instead fixed in methanol for 10 mins at −20°C. The fixed brains were then washed 3Xin 1X PBS, then incubated for 1.5 hr in blocking buffer (1X PBS, 1% BSA, 0.5% Goat Serum, 0.2% Triton X-100). Brain preparations were first incubated for 2 hr at RT with the primary antibodies, and then 2 hr at RT with the fluorescently-conjugated secondary antibodies. The primary antibodies used included; mouse anti-hFMRP (Chemicon International MAB2160; 1:500), mouse anti-dFMRP (Abcam 6A15; 1:62.5), mouse anti-Myc (Developmental Studies Hybridoma Bank 9E10; 1:15), rabbit anti-Staufen (St Johnston et al., 1991; 1:400), rabbit anti-DC0/PKA-C (Crittenden et al., 1998; 1:500), Rat anti-Rugose (Volders et al., 2012; 1:500), Rabbit anti-Phospho-PKA-C (Androschuket al., 2018:1:20) and 488-conjugated goat anti-HRP (Jackson ImmunoResearch 123-545-021; 1:250). Fluorescently-conjugated primary and secondary antibodies used included; FITC-conjugated goat anti-GFP (Abcam ab6662), Alexa Fluor 555 donkey anti-mouse (Invitrogen A31570), Alexa Fluor 488 goat anti-rabbit (Invitrogen A11008), Alexa Fluor 555 donkey anti-rabbit (A31572), Alexa Fluor 488 donkey anti-rat (A21208), Alexa Fluor 546 goat anti-rat (A11081) and Alexa Fluor 568 goat anti-mouse (Invitrogen A11004), all at 1:500. The SYTO RNA-Select green fluorescent cell stain (Molecular Probes S32703) was used following the manufacture protocol for fixed eukaryotic cells. For Thioflavin T (ThT; Abcam ab120751) labeling, acutely dissected brains were incubated in 100 mM ThT and DRAQ5 (Thermo Scientific 62254; 1:500) in PBS for 10 mins. Imaging was done on a Zeiss LSM 510 Meta confocal microscope using Plan NeoFluar 20X (0.5 NA), Plan NeoFluar 40X oil-immersion (1.3 NA) or Plan Apochromat 63X oil-immersion (1.4 NA) objectives.

QUANTIFICATION AND STATISTICAL ANALYSES

Image Analyses—All image analyses was conducted in ImageJ and ImageJ FIJI. For dFMRP intensity measurements, two ROIs were defined; 20 μm radius circleof the MB Kenyon Cell somata, and a 40 μm radius circle including the surrounding brain somata. PKA-SPARK fluorescence or P-PKA-C labeling was used to highlight MB Kenyon Cells for analysis of the first 3–5 optical sections, with adjacent brain cells similarly analyzed. For assembly long and short axis measurements, single slices (Figure 4) or Z-projections (Figure S5) were analyzed with the Freehand Line tool of ImageJ. For colocalization analyses, ImageJ FIJI plugin Coloc2 was used together with Man-ders' Colocalization Coefficient (MCC), with auto-threshold to assess co-occurrence, and Pearson's Correlation Coefficient (PCC), both with and without auto-threshold to assess correlation. For pixel-by-pixel visualization testing pixel value intensities from multiple immunolabeled fluorophores, the lookup table Magenta Hot was used with maximum value pixels removed.

Statistical Analyses—All statistical analyses were conducted using GraphPad Prism (version 8). All compared groups were always processed in parallel at the same time and under identical conditions. All compared samples were imaged at identical settings, with

image analysis conduced in parallel using ImageJ. Female and male sample numbers were kept consistent between all compared groups. Normalized data were taken from the ratio of values to control group averages, and reproducibility and validation were tested through the use of mutiple trials, antibody staining and antibody counterstaining when possible. Datasets passing normality tests were compared with two-tailed Welch's t tests or Brown-Forsythe and Welch ANOVA tests (shortened to Welch ANOVA), while all other datasets were compared with Mann-Whitney or Kruskal-Wallis tests. Statistics in the text and error bars in charts display the standard error of the mean, SEM.

Supplementary Material

Refer to Web version on PubMed Central for supplementary material.

ACKNOWLEDGMENTS

We are indebted to the Bloomington Drosophila Stock Center (Indiana University, USA) for genetic lines and the Developmental Studies Hybridoma Bank (University of Iowa, USA) for antibodies. We are grateful to Peng Jin (Emory University, USA) and Xiaokun Shu (University of California, San Francisco, USA) for lines and Daniel St Johnston (Cambridge University, UK) and Dan Kalderon (Columbia University, USA) for antibodies. We thank members of the Broadie Lab for technical input and Carolina Sears for use of a diffuser-modified remote heater. This work is supported by National Institutes of Health grant MH084989 (to K.B.) and the Vanderbilt Postdoctoral Training Program in Functional Neurogenomics (5T32MH065215 to J.C.S.).

REFERENCES

Alberti S, Gladfelter A, and Mittag T (2019). Considerations and Challenges in Studying Liquid-Liquid Phase Separation and Biomolecular Condensates. Cell 776,419–434.

Androschuk A, He RX, Weber S, Rosenfelt C, and Bolduc FV (2018). Stress Odorant Sensory Response Dysfunction in Drosophila Fragile X Syndrome Mutants. Front. Mol. Neurosci 11, 242. [PubMed: 30135642]

Barbee SA, Estes PS, Cziko A-M, Hillebrand J, Luedeman RA, Coller JM, Johnson N, Howlett IC, Geng C, Ueda R, et al. (2006). Staufen-and FMRP-containing neuronal RNPs are structurally and functionally related to somatic P bodies. Neuron 52, 997–1009. [PubMed: 17178403]

Berry-Kravis E, and Huttenlocher PR (1992). Cyclic AMP metabolism in fragile X syndrome. Ann. Neurol 31, 22–26. [PubMed: 1371909]

Berry-Kravis E, Hicar M, and Ciurlionis R (1995). Reduced cyclicAMP production infragileXsyndrome: cytogeneticand molecular correlations. Pediatr. Res 38, 638–643. [PubMed: 8552427]

Blice-Baum AC, and Mihailescu M-R (2014). Biophysical characterization of G-quadruplex forming FMR1 mRNA and of its interactions with different fragile X mental retardation protein isoforms. RNA 20, 103–114. [PubMed: 24249225]

Blum AL, Li W, Cressy M, and Dubnau J (2009). Short-and long-term memory in Drosophila require cAMP signaling in distinct neuron types. Curr. Biol 19, 1341–1350. [PubMed: 19646879]

Brengues M, Teixeira D, and Parker R (2005). Movement of eukaryotic mRNAs between polysomes and cytoplasmic processing bodies. Science 310, 486–89. [PubMed: 16141371]

Chong PA, Vernon RM, and Forman-Kay JD (2018). RGG/RG Motif Regions in RNA Binding and Phase Separation. J. Mol. Biol 430, 4650–4665. [PubMed: 29913160]

Coffee RL (2011). Insights into the Human Fragile X Syndrome Gene Family Using Drosophila melanogaster. PhD thesis (Vanderbilt University).

Coffee B, Ikeda M, Budimirovic DB, Hjelm LN, Kaufmann WE, and Warren ST (2008). Mosaic FMR1 deletion causes fragile X syndrome and can lead to molecular misdiagnosis: a case report and review ofthe literature. Am. J. Med. Genet. A 146A, 1358–1367. [PubMed: 18412117]

Coffee RL Jr., Tessier CR, Woodruff EA 3rd, and Broadie K (2010). Fragile X mental retardation protein has a unique, evolutionarily conserved neuronal function not shared with FXR1P or FXR2P. Dis. Model. Mech 3, 471–485. [PubMed: 20442204]

Collins SC, Bray SM, Suhl JA, Cutler DJ, Coffee B, Zwick ME, and Warren ST (2010). Identification of novel FMR1 variants by massively parallel sequencing in developmentally delayed males. Am. J. Med. Genet. A 152A, 2512–2520. [PubMed: 20799337]

Connolly JB, Roberts IJ, Armstrong JD, Kaiser K, Forte M, Tully T, and O'Kane CJ (1996). Associative learning disrupted by impaired Gs signaling in Drosophila mushroom bodies. Science 274, 2104–2107. [PubMed: 8953046]

Crittenden JR, Skoulakis EMC, Han KA, Kalderon D, and Davis RL (1998). Tripartite mushroom body architecture revealed by antigenic markers. Learn. Mem 5, 38–51. [PubMed: 10454371]

Darnell JC, Van Driesche SJ, Zhang C, Hung KYS, Mele A, Fraser CE, Stone EF, Chen C, Fak JJ, Chi SW, et al. (2011). FMRP stalls ribo-somal translocation on mRNAs linked to synaptic function and autism. Cell 146,247–261. [PubMed: 21784246]

Davis JK, and Broadie K (2017). Multifarious Functions of the Fragile X Mental Retardation Protein. Trends Genet. 33, 703–714. [PubMed: 28826631]

Doll CA, and Broadie K (2015). Activity-dependent FMRP requirements in development of the neural circuitry of learning and memory. Development 142,1346–1356. [PubMed: 25804740]

Doll CA, and Broadie K (2016). Neuron class-specific requirements for Fragile X Mental Retardation Protein in critical period development of calcium signaling in learning and memory circuitry. Neurobiol. Dis 89, 76–87. [PubMed: 26851502]

Doll CA, Vita DJ, and Broadie K (2017). FragileXMental Retardation Prtein Requirements in Activity-Dependent Critical Period Neural Circuit Refinement. Curr. Biol 27, 2318–2330.e3. [PubMed: 28756946]

Duffy JB (2002). GAL4 system in Drosophila: a fly geneticist's Swiss army knife. Genesis 34, 1–15. [PubMed: 12324939]

Gareau C, Martel D, Coudert L, Mellaoui S, and Mazroui R (2013a). Characterization ofFragileXMental Retardation Protein granulesformation and dnamics in Drosophila. Biol. Open 2, 68–81. [PubMed: 23336078]

Gareau C, Houssin E, Martel D, Coudert L, Mellaoui S, Huot M-E, Laprise P, and Mazroui R (2013b). Characterization offragileXmental retadation protein recruitment and dynamics in Drosophila stress granules. PLoS ONE 8, e55342. [PubMed: 23408971]

Halls ML, and Cooper DMF (2017). Adenylyl cyclase signalling complexes -Pharmacological challenges and opportunities. Pharmacol. Ther 172, 171–180. [PubMed: 28132906]

Hervas R, Rau MJ, Park Y, Zhang W, Murzin AG, Fitzpatrick JAJ, Scheres SHW, and Si K (2020). Cryo-EM structure ofa neuronal functional amyloid implicated in memory persistence in Drosophila. Science 367, 1230–1234. [PubMed: 32165583]

Hu Y, Chen Z, Fu Y, He Q, Jiang L, Zheng J, Gao Y, Mei P, Chen Z, and Ren X (2015). The amino-terminal structure of human fragile X mental retardation protein obtained using precipitant-immobilized imprinted polynmers. Nat. Commun 6, 6634. [PubMed: 25799254]

Kang DE, and Woo JA (2019). Cofilin, a Master Node Regulating Cytoskel-etal Pathogenesis in Alzheimer's Disease. J. Alzheimers Dis 72 (s1), S131–S144. [PubMed: 31594228]

Kato M, Han TW, Xie S, Shi K, Du X, Wu LC, Mirzaei H, Goldsmith EJ, Longgood J, Pei J, et al. (2012). Cell-free formation of RNA granules: low complexity sequence domains form dynamic fibers within hydrogels. Cell 149, 753–767. [PubMed: 22579281]

Kelley DJ, Davidson RJ, Elliott JL, Lahvis GP, Yin JCP, and Bhatta-charyya A (2007). The cyclic AMP cascade is altered in the fragile X nervous system. PLoS ONE 2, e931. [PubMed: 17895972]

Kiger JA Jr., Eklund JL, Younger SH, and O'Kane CJ (1999). Transgenic inhibitors identify two roles for protein kinase A in Drosophila development. Genetics 152, 281–290. [PubMed: 10224260]

Kim HJ, Kim NC, Wang Y-D, Scarborough EA, Moore J, Diaz Z, Ma-cLea KS, Freibaum B, Li S, Molliex A, et al. (2013). Mutations in prion-like domains in hnRNPA2B1 and hnRNPA1 cause multisystem proteinopathy and ALS. Nature 495, 467–473. [PubMed: 23455423]

Laker RC, Xu P, Ryall KA, Sujkowski A, Kenwood BM, Chain KH, Zhang M, Royal MA, Hoehn KL, Driscoll M, et al. (2014). A novel Mito-Timer reporter gene for mitochondrial content, structure, stress, and damage in vivo. J. Biol. Chem 289, 12005–12015. [PubMed: 24644293]

Lanuza MA, Just-Borras L, Hurtado E, Cilleros-Mane V, Tomas M, Garcia N, and Tomas J (2019). The Impact of Kinases in Amyotrophic Lateral Sclerosis at the Neuromuscular Synapse: Insights into BDNF/TrkB and PKC Signaling. Cells 8, 1578.

Lee D (2015). Global and local missions ofcAMPsignaling in neural plasticity, learning, and memory. Front. Pharmacol 6, 161. [PubMed: 26300775]

Lee VM-Y, Goedert M, and Trojanowski JQ (2001). Neurodegenerative tauopathies. Annu. Rev. Neurosci 24, 1121–1159. [PubMed: 11520930]

Lin M-D, Jiao X, Grima D, Newbury SF, Kiledjian M, and Chou T-B (2008). Drosophila processing bodies in oogenesis. Dev. Biol 322, 276–288. [PubMed: 18708044]

Ling S-C, Polymenidou M, and Cleveland DW (2013). Converging mechanisms in ALS and FTD: disrupted RNA and protein homeostasis. Neuron 79, 416–438. [PubMed: 23931993]

Luo Y, Na Z, and Slavoff SA (2018). P-Bodies: Composition, Properties, and Functions. Biochemistry 57, 2424–2431. [PubMed: 29381060]

Mateju D, Franzmann TM, Patel A, Kopach A, Boczek EE, Maharana S, Lee HO, Carra S, Hyman AA, and Alberti S (2017). An aberrant phase transition of stress granules triggered by misfolded protein and prevented by chaperone function. EMBO J. 36, 1669–1687. [PubMed: 28377462]

Mazroui R, Huot M-E, Tremblay S, Filion C, Labelle Y, and Khandjian EW (2002). Trapping of messenger RNA by FragileXMental Retardation protein into cytoplasmic granules induces translation repression. Hum. Mol. Genet 11, 3007–3017. [PubMed: 12417522]

Mazroui R, Huot ME, Tremblay S, Boilard N, Labelle Y, and Khandjian EW (2003). Fragile X Mental Retardation protein determinants required for its association with polyribosomal mRNPs. Hum. Mol. Genet 12, 3087–3096. [PubMed: 14532325]

McGuire SE, Le PT, Osborn AJ, Matsumoto K, and Davis RL (2003). Spatiotemporal rescue of memory dysfunction in Drosophila. Science 302, 1765–1768. [PubMed: 14657498]

Molliex A, Temirov J, Lee J, Coughlin M, Kanagaraj AP, Kim HJ, Mittag T, and Taylor JP (2015). Phase separation by low complexity domains promotes stress granule assembly and drives pathological fibrillization. Cell 163, 123–133. [PubMed: 26406374]

Myrick LK, Nakamoto-Kinoshita M, Lindor NM, Kirmani S, Cheng X, and Warren ST (2014). Fragile X syndrome due to a missense mutation. Eur. J. Hum. Genet 22, 1185–1189. [PubMed: 24448548]

Myrick LK, Deng P-Y, Hashimoto H, Oh YM, Cho Y, Poidevin MJ, Suhl JA, Visootsak J, Cavalli V, Jin P, et al. (2015a). Independent role for presynaptic FMRP revealed by an FMR1 missense mutation associated with intellectual disability and seizures. Proc. Natl. Acad. Sci. USA 112, 949–956. [PubMed: 25561520]

Myrick LK, Hashimoto H, Cheng X, and Warren ST (2015b). Human FMRP contains an integral tandem Agenet (Tudor) and KH motif in the amino terminal domain. Hum. Mol. Genet 24, 1733–1740. [PubMed: 25416280]

Nil Z, Hervas R, Gerbich T, Leal P, Yu Z, Saraf A, Sardiu M, Lange JJ, Yi K, Unruh J, et al. (2019). Amyloid-like Assembly Activates a Phosphatase in the Developing Drosophila Embryo. Cell 178, 1403–1420.e21. [PubMed: 31491385]

Ozdilek BA, Thompson VF, Ahmed NS, White CI, Batey RT, and Schwartz JC (2017). Intrinsically disordered RGG/RG domains mediate degenerate specificity in RNA binding. Nucleic Acids Res. 45, 7984–7996. [PubMed: 28575444]

Ramachandran V, Shah KH, and Herman PK (2011). The cAMP-dependent protein kinase signaling pathway is a key regulator of P body foci formation. Mol. Cell 43, 973–981. [PubMed: 21925385]

Ramos A, Hollingworth D, Adinolfi S, Castets M, Kelly G, Frenkiel TA, Bardoni B, and Pastore A (2006). The structure of the N-terminal domain of the fragile X mental retardation protein: a platform for protein-protein interaction. Structure 14, 21–31. [PubMed: 16407062]

Schaeffer C, Bardoni B, Mandel JL, Ehresmann B, Ehresmann C, and Moine H (2001). The fragile X mental retardation protein binds specifically to its mRNA via a purine quartet motif. EMBO J. 20, 4803–4813. [PubMed: 11532944]

Sears JC, and Broihier HT (2016). FoxO regulates microtubule dynamics and polarity to promote dendrite branching in Drosophila sensory neurons. Dev. Biol 418, 40–54. [PubMed: 27546375]

Sears JC, Choi WJ, and Broadie K (2019). Fragile X Mental Retardation Protein positively regulates PKA anchor Rugose and PKA activity to control actin assembly in learning/memory circuitry. Neurobiol. Dis 127, 53–64. [PubMed: 30771457]

Si K, and Kandel ER (2016). The Role of Functional Prion-Like Proteins in the Persistence of Memory. Cold Spring Harb. Perspect. Biol 8, a021774. [PubMed: 27037416]

St Johnston D, Beuchle D, and Nusslein-Volhard C (1991). Staufen, a gene required to localize maternal RNAs in the Drosophila egg. Cell 66, 51–63. [PubMed: 1712672]

Taylor SS, Zhang P, Steichen JM, Keshwani MM, and Kornev AP (2013). PKA: lessons learned after twenty years. Biochim. Biophys. Acta 1834, 1271–1278. [PubMed: 23535202]

Tessier CR, and Broadie K (2008). Drosophila fragile X mental retardation protein developmentally regulates activity-dependent axon pruning. Development 135, 1547–1557. [PubMed: 18321984]

Tudisca V, Recouvreux V, Moreno S, Boy-Marcotte E, Jacquet M, and Portela P (2010). Differential localization to cytoplasm, nucleus or P-bodies of yeast PKA subunits under different growth conditions. Eur. J. Cell Biol 89, 339–348. [PubMed: 19804918]

Verkerk AJ, Pieretti M, Sutcliffe JS, Fu YH, Kuhl DP, Pizzuti A, Reiner O, Richards S, Victoria MF, Zhang FP, et al. (1991). Identification ofagene (FMR-1)containing a CGG repeat coincident with a breakpoint cluster region exhibiting length variation in fragile X syndrome. Cell 65, 905–914. [PubMed: 1710175]

Vita DJ, and Broadie K (2017). ESCRT-III MembraneTrafficking Misregula-tion Contributes To Fragile X Syndrome Synaptic Defects. Sci. Rep 7, 8683. [PubMed: 28819289]

Volders K, Scholz S, Slabbaert JR, Nagel AC, Verstreken P, Creemers JWM, Callaerts P, and Schwarzel M (2012). Drosophila rugose is a functional homolog ofmammalian Neurobeachin and affects synapticarchitecture, brain morphology, and associative learning. J. Neurosci 32, 15193–15204. [PubMed: 23100440]

Wang Q-P, Lin YQ, Lai M-L, Su Z, Oyston LJ, Clark T, Park SJ, Khuong TM, Lau M-T, Shenton V, et al. (2020). PGC1 a Controls Sucrose Taste Sensitization in Drosophila. Cell Rep. 31, 107480. [PubMed: 32268099]

Weber SC, and Brangwynne CP (2012). Getting RNA and protein in phase. Cell 149, 1188–1191. [PubMed: 22682242]

Yeboah F, Kim T-E, Bill A, and Dettmer U (2019). Dynamic behaviors of a-synuclein and tau in the cellularcontext: New mechanistic insights and therapeutic opportunities in neurodegeneration. Neurobiol. Dis 132, 104543. [PubMed: 31351173]

Zars T, Fischer M, Schulz R, and Heisenberg M (2000). Localization of a short-term memory in Drosophila. Science 288, 672–675. [PubMed: 10784450]

Zhang YQ, Bailey AM, Matthies HJG, Renden RB, Smith MA, Speese SD, Rubin GM, and Broadie K (2001). DrosophilafragileX-related gene regulates the MAP1B homolog Futsch to control synaptic structure and function. Cell 107, 591–603. [PubMed: 11733059]

Zhang Q, Huang H, Zhang L, Wu R, Chung C-I, Zhang S-Q, Torra J, Schepis A, Coughlin SR, Kornberg TB, and Shu X (2018). Visualizing Dynamics ofCell Signaling In Vivo with a Phase Separation-Based Kinase Reporter. Mol. Cell 69, 334–346.e4. [PubMed: 29307513]

Highlights

- Human and *Drosophila* FMRP drive PKA activation in learning/memory circuit neurons
- PKA activity suppresses *human/Drosophila* FMRP levels via a negative feedback loop
- Patient-derived R140Q redirects PKA activation to dendrites and disrupts circuitry
- The FMRP mRNA-binding RGG box domain suppresses cytosolic fibrillar partitioning

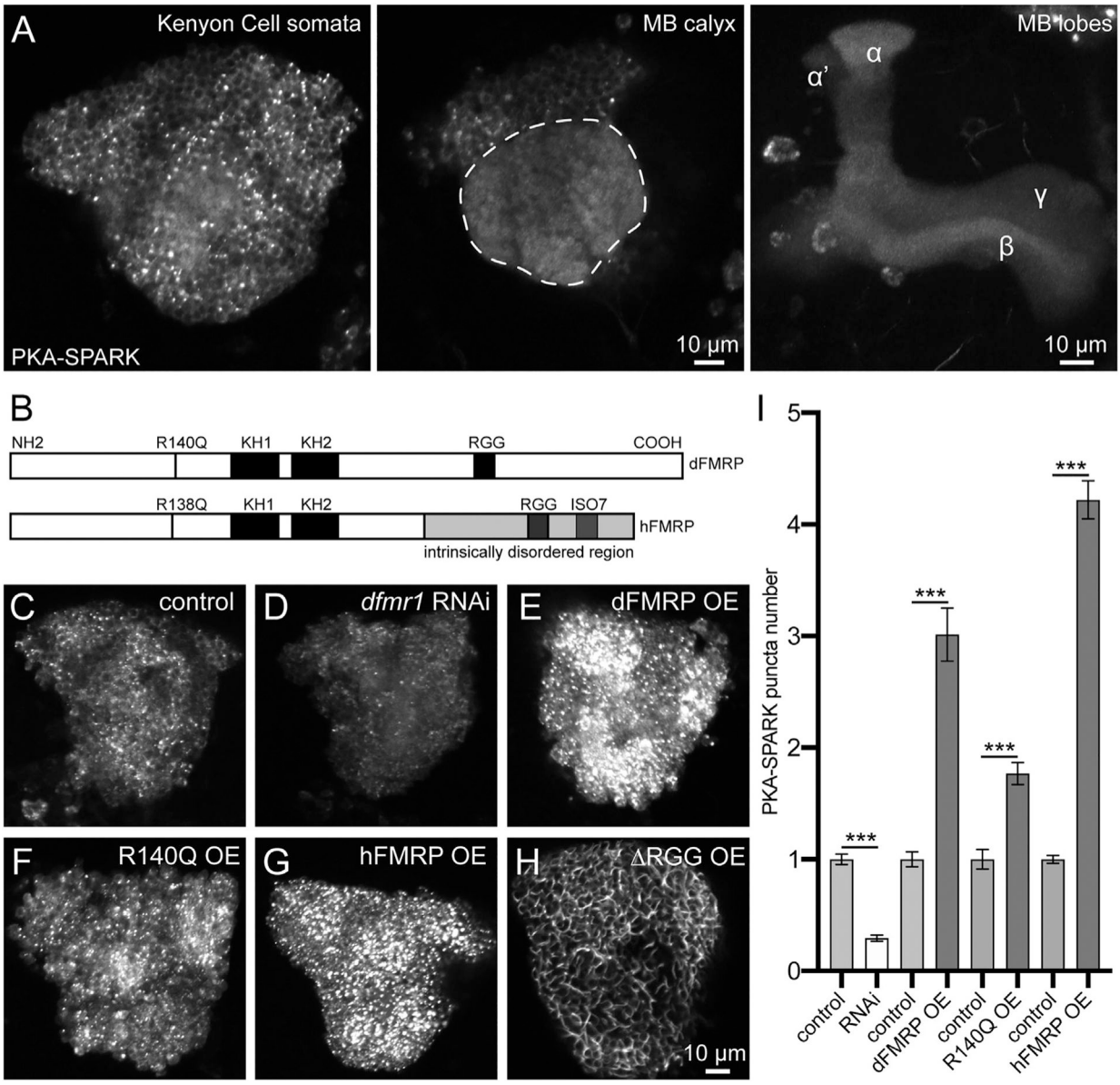

Figure 1. FMRP Variants Promote PKA Activity in the MB

(A) OK107-Gal4 driving UAS-PKA-SPARK in KC somata (left), calyx (center, dotted outline), and axon lobes (right).

(B) Drosophila and human FMRP with mutations and isoforms.

(C-H) KC PKA-SPARK images in the w^{1118} background (C) or with UAS-dfmr1 RNAi (D), UAS-dFMRP OE (E), UAS-dFMRP [R140Q] (F), UAS-hFMRP OE (G), and UAS-hFMRP [ΔRGG] (H).

(I) Quantification of normalized PKA-SPARK punctum number, indicating mean ± SEM. n = 12–17 KC fields. Statistics show two-tailed unpaired t tests with Welch's correction. Significance: ***p < 0.001.

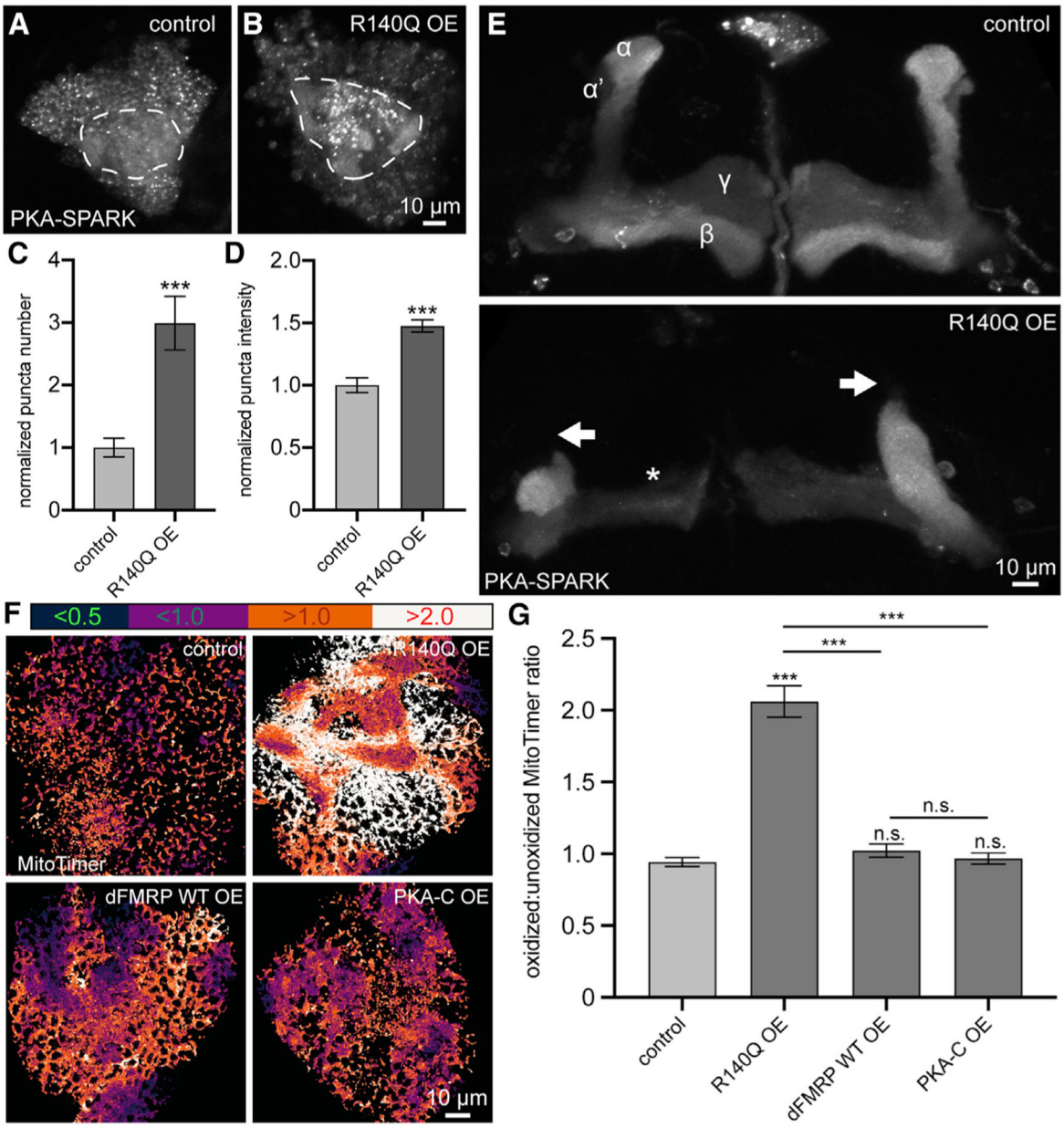

Figure 2. FMRP R140Q Promotes MB Calyx PKA Activity and MB Axon Defects

(A and B)MB calyx (dashed circle) with OK107-Gal4 driving PKA-SPARK in w^{1118} (A) and with dFMRP-R140Q OE (B).

(C and D) Quantification of normalized PKA-SPARK punctum number (C) and punctum fluorescence intensity (D) showing mean ± SEM. n = 13–14 KC fields.

(E) Arrows show missing MB α/α' lobes, and an asterisk marks a thin γ lobe.

(F) OK107-Gal4 driving UAS-MitoTimer in w^{1118} (top left) with UAS-dFMRP (R140Q) (top right), UAS-WT hFMRP (bottom left), and UAS-PKA-C (bottom right) in KCs. Images are color-coded to show the oxidation state (R:G ratio).

(G) Quantification of R:G ratios, showing mean ± SEM.

n = 20–34 KC fields. Statistics show unpaired t tests with Welch's correction and Welch ANOVA. Significance: ***$p < 0.001$; not significant (n.s.), $p > 0.05$.

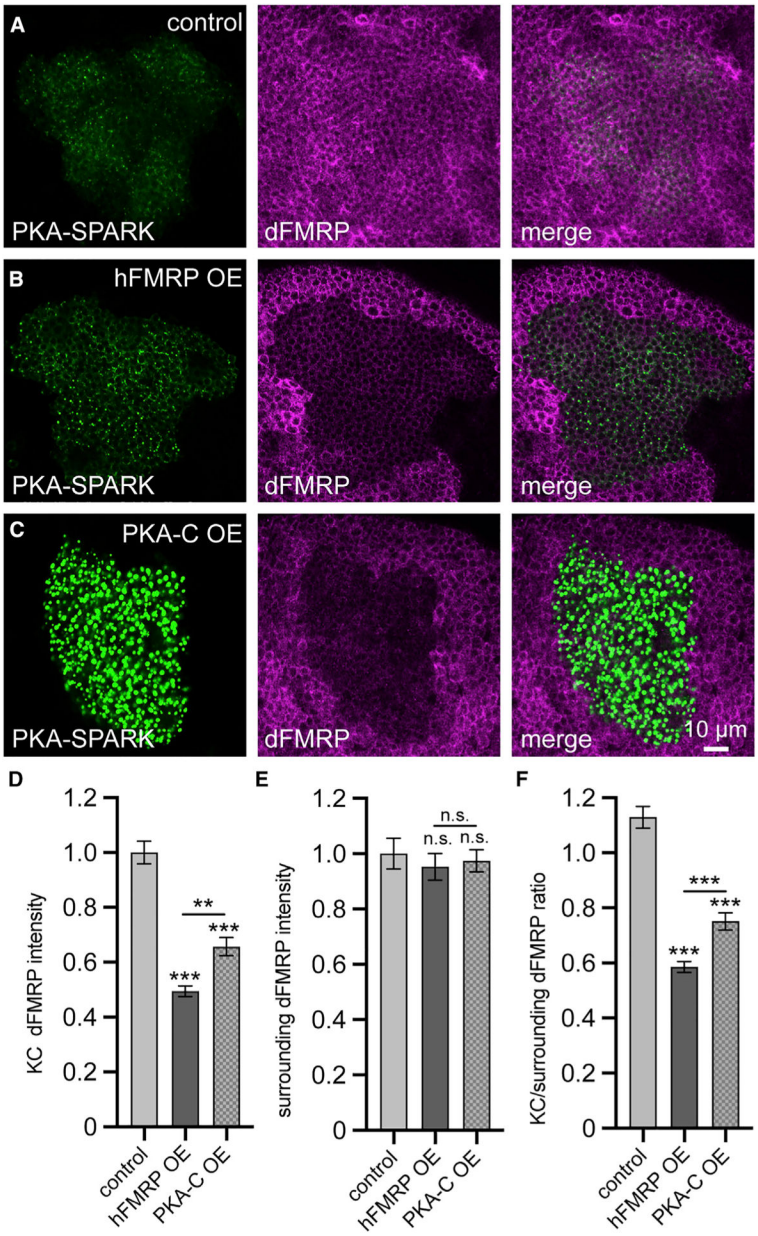

Figure 3. Transgenic hFMRP and PKA Activation Limit MB dFMRP Levels

(A-C) KC brain regions with OK107-Gal4 driving PKA-SPARK (green) co-labeled for anti-dFMRP (magenta) in w^{1118} (A), with hFMRP OE (B), or PKA-C OE (C).

(D-F) Quantification of normalized dFMRP intensity in KC somata (D), normalized dFMRP intensity in surrounding brain somata (E), and the KC/surrounding somata ratio (F), showing mean ± SEM. n = 12–18 KC/surround fields. Statistics show Welch ANOVA with Dunnett's multiple comparisons tests. Significance: ***p < 0.001; **p < 0.01; n.s., p > 0.05.

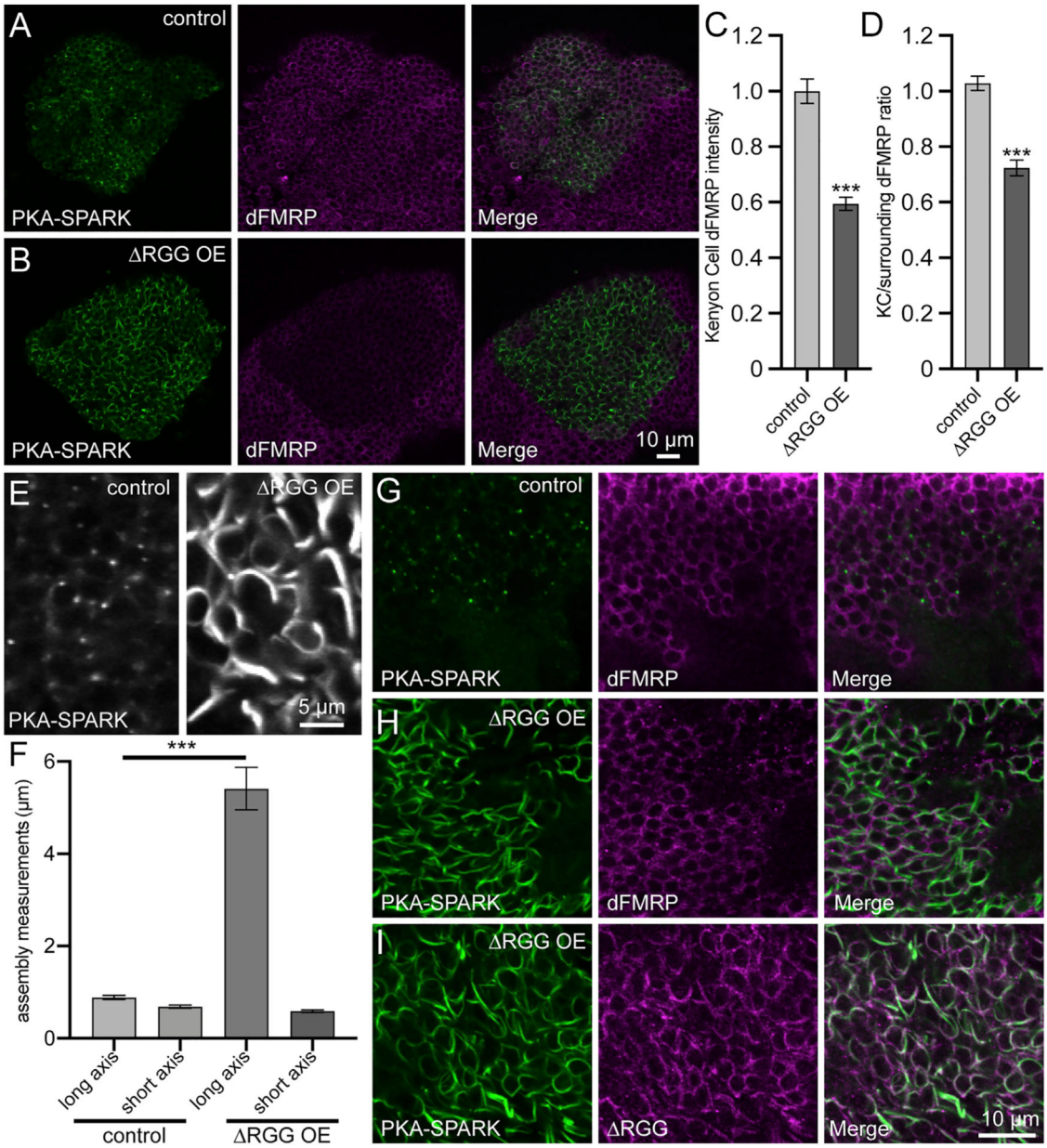

Figure 4. hFMRP-ΔRGG-Suppressing dFMRP Colocalizes in PKA-SPARK Aggregates

(A and B) OK107-Gal4 driving PKA-SPARK (green) co-labeled for anti-dFMRP (magenta) in w^{1118} (A) and with hFMRP-ΔRGG (B).

(C and D) Quantification of normalized dFMRP intensity in KCs (C) and KC/surrounding somata ratio (D), showing mean ± SEM. n = 13 KC/surround fields.

(E) PKA-SPARK fluorescence with OK107-Gal4 driving PKA-SPARK in w^{1118} (left) and hFMRP-ΔRGG (right).

(F) Quantification of PKA-SPARK assembly long/short axes, showing mean ± SEM. n = 30–40 axes.

(G-I) OK107-Gal4 driving PKA-SPARK in KCs, immunolabeled for PKA-SPARK (green), dFMRP (magenta, G and H), and hFMRP-ΔRGG::Myc (magenta, I). Statistics are from

unpaired t tests with Welch's correction (C and D) and Kruskal-Wallis tests (F). Significance: ***$p < 0.001$.

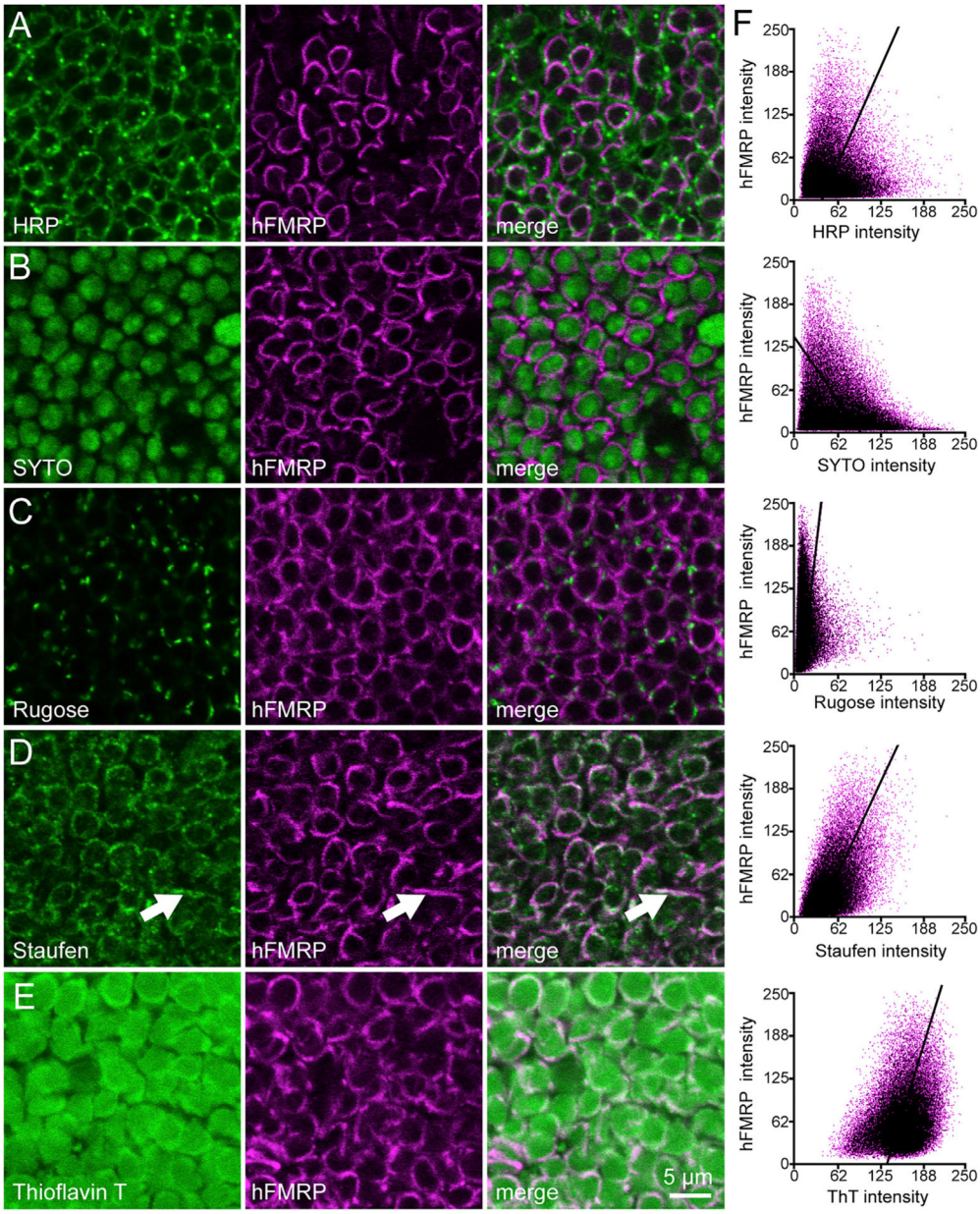

Figure 5. hFMRP-ΔRGG Colocalizes Processing Bodies and Fibrillar Aggregates

(A) KC somata co-labeled with anti-horseradish peroxidase (HRP) to mark neuronal membranes (green), with OK107-Gal4 driving hFMRP-ΔRGG (magenta).

(B) KCs labeled with SYTO RNA-Select to mark KC nuclei (green) and hFMRP-ΔRGG (magenta).

(C) KCs labeled for Rugose (green) and hFMRP-ΔRGG (magenta).

(D) KCs labeled for Staufen (green) to mark RNPs and hFMRP-ΔRGG (magenta).

(E) KCs labeled for ThT (green) to mark aggregates and hFMRP-ΔRGG (magenta).

(F) Co-occurrence intensity of each marker from (A)-(E).

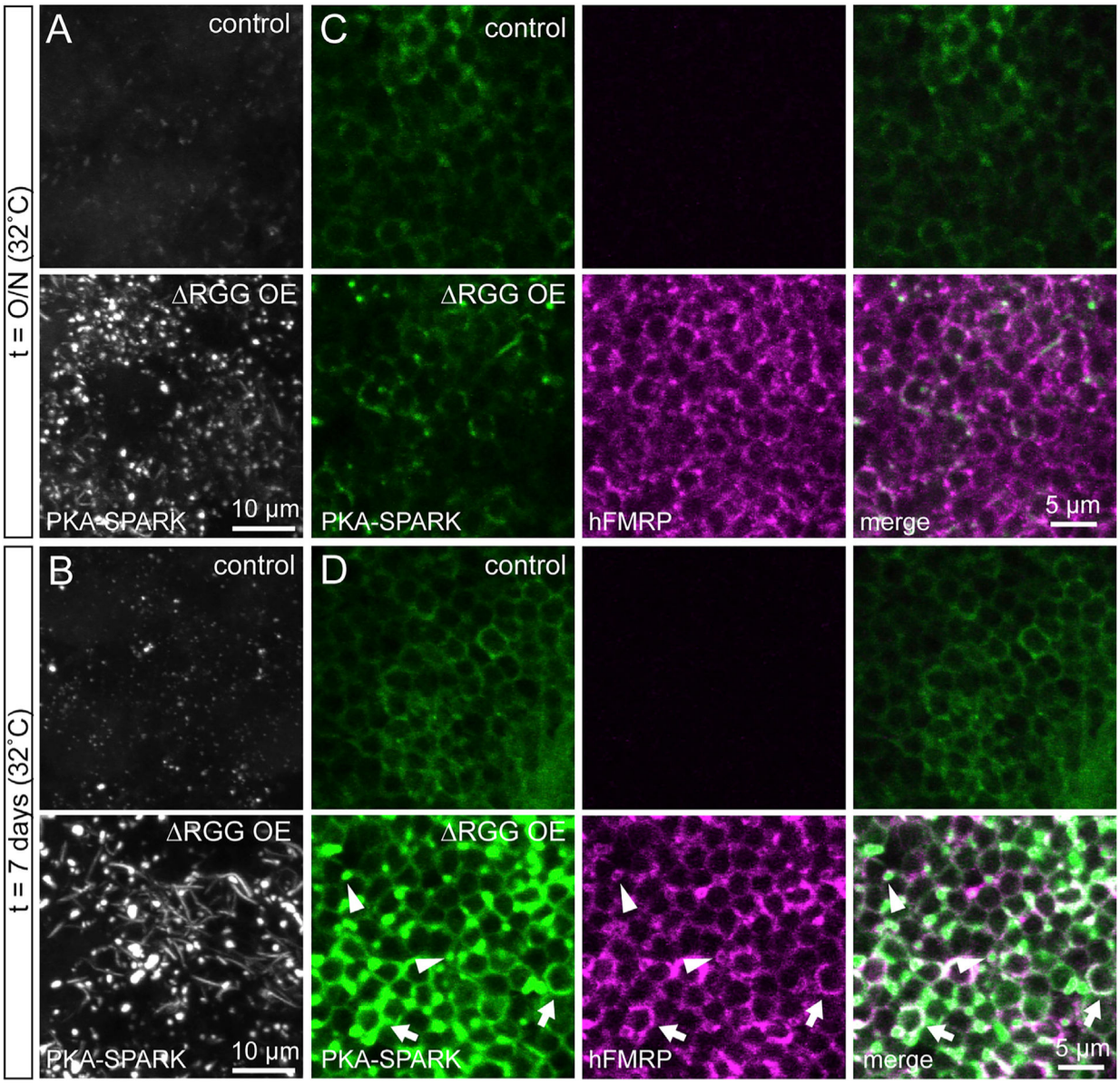

Figure 6. hFMRP-ΔRGG Promotes Spherical Puncta Prior to Forming Elongated Fibrils

(A and B) KCs with OK107-Gal4 driving PKA-SPARK in w^{1118} (top panel) and with hFMRP-ΔRGG (bottom panel), with $Gal80^{ts}$ to prevent Gal4 transcriptional activation overnight (O/N; A) or 1 week at 32°C (B).

(C and D) The same conditions co-labeled for PKA-SPARK (green, left) and anti-hFMRP (magenta, center). Arrowheads mark hFMRP surrounding PKA-SPARK puncta. Arrows mark fibrillar assemblies with co-occurrence.

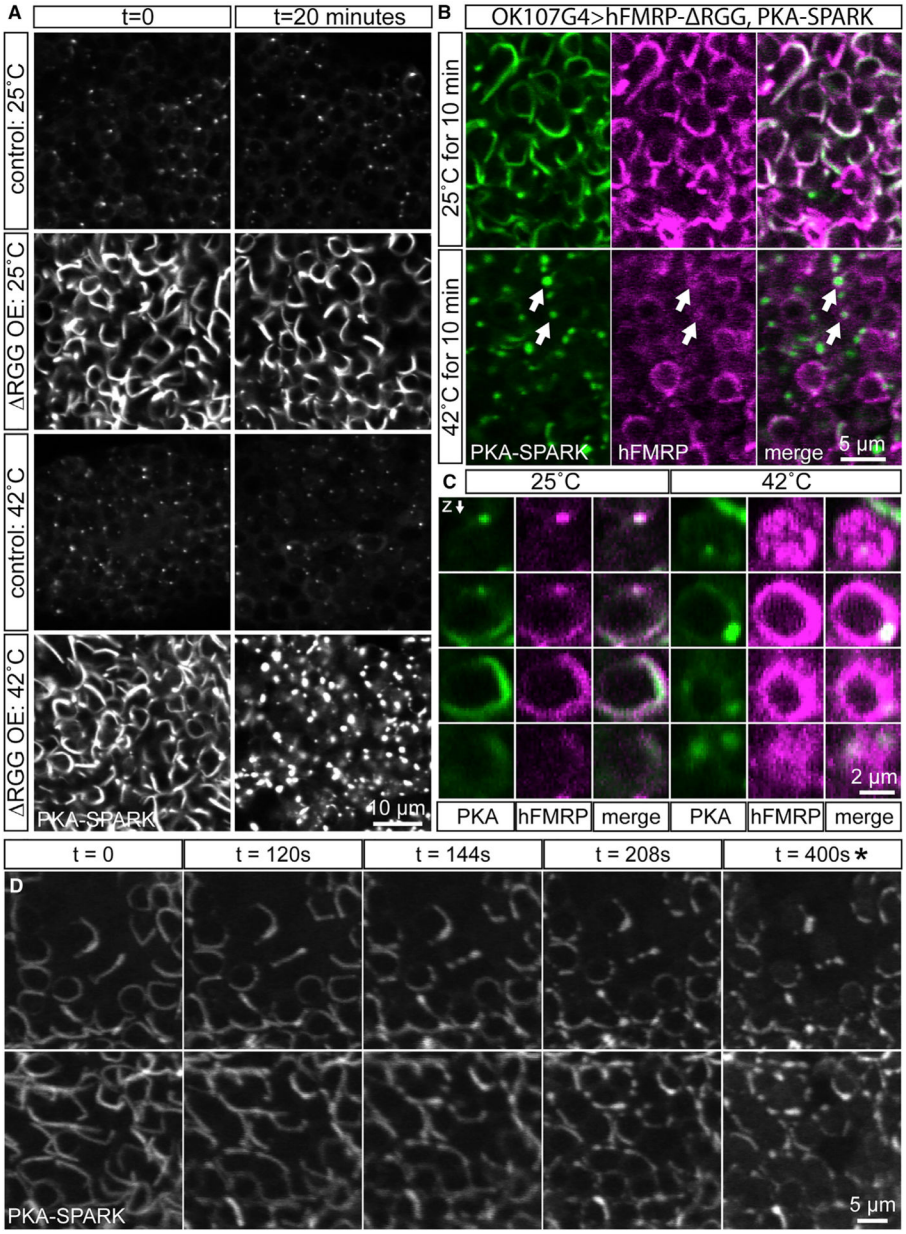

Figure 7. hFMRP-ΔRGG Fibrillar Assemblies Disperse at Elevated Temperatures

(A) KCs expressing PKA-SPARK before/after 20 min at 25°C or 42°C in control (rows 1 and 3) and with hFMRP-ΔRGG (rows 2 and 4).

(B) KCs labeled for PKA-SPARK (green) and anti-hFMRP (magenta) with hFMRP-ΔRGG at 25°C or 42°C for 10 min.

(C) High-magnification images of individual KCs in adjacent z stack slices.

(D) Continuous imaging in hFMRP-ΔRGG animals heated for5min andthen imaged for8min. Thetop and bottom panelscorrespond totop and bottom regionsof interest (ROIs) in Video S2. Time points shown are between t = 0 and t = 400 s (no heat, *), with heat applied from t = 0 and t = 300 s.

KEY RESOURCES TABLE

REAGENT or RESOURCE	SOURCE	IDENTIFIER
Antibodies		
488-conjugated goat anti-HRP	Jackson ImmunoResearch	123-545-021, RRID:AB_2338965
FITC-conjugated goat anti-GFP	Abcam	ab6662, RRID:AB_305635
Rabbit anti-PKA-C DC0	Daniel Kalderon	DC0, RRID: AB_2314291
Rabbit anti-phospho-PKA-C (T198)	Abcam	ab118531, RRID: AB_10898971
Mouse anti-MYC	Developmental Studies Hybridoma Bank	9E 10, RRID: AB_2266850
Mouse anti-dFMRP	Abcam	6A15, ab10299, RRID: AB_297038
Mouse anti-hFMRP	Chemicon International	MAB2160, RRID: AB_2283007
Rat anti-Rugose	Martin Schwarzel	Volders et al., 2012; RRID: AB_2570006
Rabbit anti-Staufen	Daniel St Johnston	St Johnston et al., 1991; RRID:AB_2569643
Rabbit anti-α-tubulin	Abcam	ab52866, RRID:AB_869989
Chemicals, Peptides, and Recombinant Proteins		
Thioflavin T	Abcam	ab120751
SYTO RNA-Select green fluorescent cell stain	Molecular Probes	S32703
DRAQ5	Thermo Scientific	62254
Experimental Models: Organisms/Strains		
w^{1118}	Bloomington *Drosophila* Stock Center	BDSC: 3605
P{y[+t7.7] = CaryP}attP2	Bloomington *Drosophila* Stock Center	BDSC: 36303
OK107-Gal4	Bloomington *Drosophila* Stock Center	BDSC: 854
201Y-Gal4	Bloomington *Drosophila* Stock Center	BDSC: 4440
UAS-PKA-SPARK	Zhang et al., 2018	N/A
UAS-$dfmr1^{WT}$	Myrick et al., 2015a	N/A
UAS-*dfmr1* RNAi	Bloomington *Drosophila* Stock Center	BDSC: 27484
UAS-$dfmr1^{R140Q}$	Myrick et al., 2015a	N/A
UAS-$hFMR1^{WT}$	This Study	N/A
UAS-MYC-$hFMR1^{\Delta RGG}$	Coffee, 2011	N/A
$dfmr1^{50M}$	Zhang et al., 2001	N/A
UAS-$MYC\text{-}hFMR1^{FL}$, $dfmr1^{50M}$	Coffee et al., 2010	N/A
UAS-$hFMR1^{\Delta RGG}$, $dfmr1^{50M}$	This Study	N/A
UAS-PKA-SPARK, $dfmr1^{50M}$	This Study	N/A
$UAS\text{-}hFMR1^{WT}$, UAS-PKA-SPARK	This Study	N/A
UAS-ERK-SPARK	Zhang et al., 2018	N/A
UAS-ERK-SPARK (T to A)	Zhang et al., 2018	N/A
UAS-MitoTimer	Bloomington *Drosophila* Stock Center	BDSC: 57323
w*; P{tubP-Gal80ts}10; TM2/TM6B, Tb1	Bloomington *Drosophila* Stock Center	BDSC: 7108
UAS-PKA-C-FLAG	Bloomington *Drosophila* Stock Center	BDSC: 35555
UAS-*rut* RNAi	Bloomington *Drosophila* Stock Center	BDSC: 27035
Software and Algorithms		

REAGENT or RESOURCE	SOURCE	IDENTIFIER
RatioMetric Analysis Macro for ImageJ	This study	https://github.com/JamesCSears/RatioMetric-Analysis-Macro-ImageJ